Coupled quantitative modeling of microstructural evolution and plastic flow during continuous dynamic recrystallization

Fei Chen[a, *], Xiao Tian[a], Guangshan Wu[a], Huajia Zhu[b], Hengan Ou[c], Zhenshan Cui[a, *]

[a] *National Engineering Research Center of Die and Mold CAD, Shanghai Jiao Tong University, 1954 Huashan Road, Shanghai, 200030, PR China*

[b] *Department of Mechanical Engineering, University College London, Torrington Place, London, WC1E 7JE, UK*

[c] *Department of Mechanical, Materials and Manufacturing Engineering, University of Nottingham, Nottingham, NG7 2RD, UK*

Highlights

- A MCA-cDRX model coupled with matrix topology deformation technique was proposed.
- The evolution of microstructures in hot-working AA7075 aluminum alloy was studied
- The macroscopic mechanical response of such materials with a high SFE was studied.
- The developed simulation framework offers an effective means for visualizing cDRX.

Abstract

Continuous dynamic recrystallization (cDRX) dominates microstructural evolution during the hot working of metallic materials with high stacking fault energy (SFE), such as aluminum alloys. However, in reality, a lack of quantitative and visual modeling of the process hinders its widespread application in the hot working process. In this study, using a recently developed multilevel cellular automaton (MCA) that integrates the newly established cell switching rules and topology deformation technique, a novel mesoscale MCA-cDRX model was constructed to investigate the evolution of both microstructures and macroscopic mechanical response in the hot working of AA7075 aluminum alloy. By considering the evolution of dislocation density and the orientation angle of the local cells as the primary clues, the plastic flow, recrystallization kinetics, features of subgrain size and high-angle grain boundaries, and influence of initial matrix characteristics on the cDRX mechanism were analyzed. The model predictions are consistent with the experimental data. Quantitative analysis confirms that the incubation time for the initiation of subgrain formation is significantly short. The fine-grain matrix and high initial volume fraction of low-angle grain boundaries can significantly accelerate the progress of cDRX owing to a stronger

*Corresponding authors: National Engineering Research Center of Die and Mold CAD, Shanghai Jiao Tong University, PR China.
E-mail addresses: feichen@sjtu.edu.cn (F. Chen); cuizs@sjtu.edu.cn (Z. Cui)

accumulation of dislocations in the dislocation cell walls through the climb and cross-slip mechanisms in the deformed aluminum alloy. The subgrain size is dependent on the Zener-Hollomon parameter. The developed simulation framework offers an effective means to allow the visualization of the cDRX.

Keywords:
A. Microstructures
A. Thermomechanical processes
B. Metallic material
C. Probability and statistics
Dynamic recrystallization

Nomenclature[2]

Symbol	Definition
δ_{sub}	Average subgrain size
r_i, δ_i	Radius of a (sub)grain and grain size of the *i*th subgrain
d_{ini}, d_{avr}	Initial and average diameters of all the grains
ρ_i	Dislocation density of the *i*th subgrain
$\rho_{matrix}, \rho_{critical}$	Matrix dislocation density and the critical dislocation density
$\tilde{\sigma}, \tilde{\varepsilon}, \dot{\tilde{\varepsilon}}$	Stress, strain, and strain rate
N_i	Total number cells belonging to the *i*th (sub)grain
V_{cel}	Volume of each cell
T	Temperature
b, k_b, μ_0	Burgers vector modulus, Boltzmann constant and shear modulus
Q_{act}, Q_b	Activation energy and grain boundary diffusion activation energy
$v_{HAB}, m_{HAB}, p_{HAB}$	Migration rate, mobility and driving force of HABs
$v_{sub}, m_{sub}, p_{sub}$	Migration rate, mobility and driving force of LABs
$v_{\max}$	Maximum grain boundary velocity
τ	Dislocation line energy
γ_β	Grain boundary energy per unit area
θ_i, θ_m	Misorientation and misorientation of HAB
υ	Poisson's ratio
δ	Grain boundary thickness
D_{ob}	Grain boundary self-diffusion coefficient
l	Average mean free path of the mobile dislocation

[2] List of abbreviations: Continuous dynamic recrystallization (cDRX); stacking fault energy (SFE); multilevel cellular automaton (MCA); dynamic recovery (DRV); dynamic recrystallization (DRX); discontinuous DRX (dDRX); low-angle grain boundaries (LABs); high-angle grain boundaries (HABs); continuous DRX (cDRX); geometric DRX (gDRX); Gourdet–Montheillet (GM); internal state variables (ISVs); visco-plastic self-consistent (VPSC); grain boundaries (GBs); cellular automaton (CA); three-dimensional (3D); multilevel CA (MCA)

E_{sub}	Subgrain boundary stored energy
Δt	The time step
ς^t	Subgrain boundary migration distance at time *t*
f^t	Grain growth fraction variable
p	Probability of finding a subgrain
P_i	State transformation probability of the cell
ϖ_i	Number of cells with the same orientation in von Neumann neighborhood
M_i	The random number from 0 to 100
$c_1, c_2, c_3, c_{20}, \beta_1, \beta_2, \chi_1, \chi_2, Kg, \lambda, \lambda_1, \xi$	Material constants

1. Introduction

Microstructure refinement by plastic deformation is a potential method for improving the mechanical properties of metallic materials. The microstructure evolution characteristics, such as dynamic recovery (DRV) and dynamic recrystallization (DRX), are intrinsically related to the stacking fault energy (SFE) level of the materials during the plastic forming process (Gottstein, 2004; Khan et al., 2011; Sakai et al., 2014; Takaki et al., 2014; Zhao et al., 2018; Li and Fu, 2019). In materials with a high SFE (e.g., aluminum alloys and α-iron), a perfect dislocation cannot easily split into two partial dislocations, and the glide, climb, and cross-slip mechanisms of perfect dislocations play a dominant role in this situation. Rapid DRV occurs readily, which effectively hinders the accumulation of sufficient dislocations to activate discontinuous DRX (dDRX) during hot deformation ($T>0.5T_m$) (Busso, 1998; Tóth et al., 2010). Consequently, subgrain boundaries that originate from the substructures of cell walls consisting of tangled dislocations are formed during deformation with only limited dislocations within them. Moreover, continuous straining progressively contributes to an increase in the misorientation of subgrain boundaries with the transformation of low-angle grain boundaries (LABs) into high-angle grain boundaries (HABs). This phenomenon is often referred to as continuous DRX (cDRX) (Gourdet and Montheillet, 2003). Furthermore, materials with a high SFE are subjected to sufficient deformation in one direction (e.g., hot rolling and torsion), which may trigger geometric DRX (gDRX) when the criterion that the grain thickness is reduced to 1~2 times the subgrain diameter is satisfied (McQueen, 2004; Huang and Logé, 2016).

Modeling and simulation of the microstructure evolution during cDRX is an effective way to optimize the hot-working parameters to achieve the desirable mechanical properties of materials with a high SFE (Khan and Meredith, 2010; Cai et al., 2020), which is also the cornerstone of understanding grain evolution during gDRX. However, as indicated by Sun et al. (2018) and Li et al. (2020), microstructure evolution during cDRX is significantly more complicated than that in dDRX and gDRX, and only a few cDRX models have been developed.

In the last two decades, some efforts have been undertaken to discover an effective way to predict the microstructure evolution during plastic deformation with cDRX (Gourdet and Montheillet, 2003; McQueen and Kassner, 2004; Fratini and Buffa, 2005; Luigi and Misiolek, 2008; Hallberg et al., 2010; Miovanni et al., 2018; Sun et al., 2018; Li et al., 2020; Chen et al., 2020; Buzolin et al., 2021). Significantly comprehensive reviews on DRX have also been performed by the top researchers in this field (Sakai et al., 2014; Huang and Logé, 2016).

The pioneering study was reported by Gourdet and Montheillet (2003), in which a physical- based cDRX model called Gourdent-Montheillet (GM) model was proposed by considering the following mechanisms: (1) the combined effects of strain hardening, DRV, and mobile boundaries on the evolution of dislocation density calculated using Laasraoui-Jonas equation (Laasraoui and Jonas, 1991); (2) the formation of subgrains with LABs, their rotation by absorbing dislocations, and the transformation of LABs into HABs; (3) the migration of HABs. The average dislocation density, area and fraction of LABs/HABs, subgrain boundary misorientation, and volume swept by the mobile boundaries were used as the internal state variables (ISVs) in the developed GM model, which could predict the refinement of an initial coarse matrix of 6060 aluminum alloy. The primary shortcoming of the GM model (McQueen and Kassner, 2004) is that impacts of grain size, dislocation density, and (sub)grain boundary misorientation on the (sub)grain rotation rate were neglected.

Hallberg et al. (2010) proposed a cDRX-based constitutive model for pure aluminum, based on dislocation dynamics and grain refinement principles. Moreover, the flow behavior and microstructure evolution while processing using the equal-channel angular pressing technique were precisely described by coupling the finite element method. Although the average grain size and dislocation density were set as the ISVs and introduced into the developed constitutive model, other specific details regarding the (sub)grains are unknown.

Recently, Sun et al. (2018) innovatively proposed a physical-based cDRX model for AA7075 alloy based on the GM model (Gourdet and Montheillet, 2003), in which the effect of the stored energy at the subgrain boundary, which primarily depends on dislocation density, subgrain size, and misorientation, on the subgrain rotation rate was considered for the first time. The microstructure and flow stress due to cDRX of AA7075 alloy during hot deformation were predicted reasonably well.

Maizza et al. (2018) extended the GM model by introducing the effects of second-phase strengthening on the dislocation density stored in the (sub)grains. Further, the initial fraction of HABs was input as a function of strain based on the fitting of the experimental data. Finally, the hot-compressed cDRX response (e.g., stress-strain curves, dislocation density, and subgrain size) of AA5052 alloy was satisfactorily predicted and verified.

Li et al. (2020) creatively improved the original GM model by considering the contributions of subgrain rotation and the transformation of LABs to HABs. The saturation values of the HAB fraction and average subgrain misorientation of AA5052 and AA7050

were predicted and verified. Recently, an ISV-based model reported by Buzolin et al. (2021) satisfactorily predicted the formation of new β-HABs in hot deformation with cDRX for Ti5553 alloy using the GM model, which demonstrates a successful attempt at the application of the GM model to describe the microstructure evolution in titanium alloy.

In general, one of the common characteristics of ISV-based models is describing the changes in the microstructure during hot deformation, by tracking the evolution of several different ISVs (e.g., phase volume fraction, subgrain size, and dislocation density), which have a clear physical meaning and should be independent of each other (Roters et al., 2000; Hallberg et al., 2010; Fan and Yang, 2011; Cho et al., 2019; Mahnken and Westermann, 2021). In such a case, the variation of each ISV with time/strain is generally updated in the form of different differential equations. The primary advantage of the ISV-based model is that it is capable of reflecting the interaction between macro-deformation behavior and microstructure evolution, and it can easily achieve the integrated prediction of flow stress and microstructure. However, one of the primary challenges of the traditional ISV-based model is that it involves a set of complex microstructure evolution mechanisms, which complicates the identification of the unknown material parameters. These models are proposed based on an assumption of homogeneous deformation in all the grains (matrix, subgrain, and recrystallized grain). However, DRX behavior varies from grain to grain, owing to their different initial orientations from a microscopic perspective. To address this issue, the GM model was further improved by Chen et al. (2020), who originally proposed a combined cDRX visco-plastic self-consistent (VPSC) model according to the classical crystal plasticity theory. The primary contribution of this work is that the role of the initial characteristics of the grain boundaries (GBs) and strain gradient on the strengthening and (sub)grain refinement were highlighted. Furthermore, an ISV-based constitutive model for AA7075 alloys was developed to quantitatively calculate the average misorientation angle, grain size, texture, and flow stress for both work hardening and softening stages. The data predicted by the cDRX-VPSC were fitted well with the experimental results.

To gain insights into the DRX mechanisms during hot working, other methods on a mesoscale and their combinations were also performed. Among them, cellular automaton (CA) is an effective way to study the DRX behavior of materials during hot working because of its high computational efficiency and flexibility. Based on the physical metallurgical principles of DRX, complex physical phenomena and morphologies can be explained by only establishing local switching rules without the need for calculating complex differential equations (Raabe, 1999, 2002; Janssens, 2010; Zheng and Raabe, 2013, Li et al., 2016). In the past few decades, the primary focus has been on developing a method for describing the microstructure evolution during dDRX with low-to-medium SFE materials, which is characterized by obvious nucleation and grain growth stages (Ding and Guo, 2001; Kugler and Turk, 2004; Yazdipour et al., 2008; Li et al., 2013; Svyetlichnyy et al., 2010, 2014; Chen et al., 2009, 2012, 2020). However, only a few mesoscale CA models for cDRX have been

developed owing to its complex mechanisms and especially because of the cross-scale interactions between dislocation multiplication and the formation of subgrains. Recently, Liu et al. (2021) first proposed a two-dimensional CA model for 2219 aluminum alloy during thermal processing based on the assumption that once the critical dislocation density (Roberts and Ahlblom, 1978) is reached, LAB migration and subgrain growth occur in the initial matrix. The predicted flow stress in the softening stage and the substructures were moderately accurate. However, this model ignores the topological characteristics of the three-dimensional (3D) grains, and does not consider the variations in the Zener-Hollomon parameter.

This study aims to develop a new mesoscale framework to track the microstructural evolution and plastic flow during hot working of the materials with high SFE, based on a model that was recently developed by Chen et al. (2021) called multilevel CA (MCA)-dDRX. The following three aspects are newly addressed:

- A 3D grain topology deformation technology is proposed, which can track the initial matrix formation after the extrusion blooming process.
- The corresponding switching rules of the local cell are defined to capture individual LAB/HAB migrations.
- The submicrostructure evolution during cDRX is visualized.

The study is structured as follows: In Section 2, the physical basis underlying the model is presented. This is followed by a description of the MCA-cDRX model in Section 3. The results of numerical simulations of the uniaxial compression processing of AA7075 aluminum alloy with regard to subgrain and misorientation distributions, cDRX kinetics, and HAB distribution are reported in Section 4. A brief concluding section contains an overall assessment of the model.

2. Physical basis of MCA-cDRX model for aluminum alloy

2.1. Physical metallurgical mechanisms

The micro-transformation mechanisms that contribute to microstructural evolution during cDRX are illustrated in Fig. 1. They can be summarized as follows.

- The formation of new subgrains with LABs: The dislocation motion and reaction lead to the formation of the initial dense dislocation wall, which promotes the formation of a geometric dislocation cell substructure. With continuous deformation and dislocation movements, the cell wall becomes clear and gradually transforms into LABs, thus forming the subgrains.
- Rotation and migration of LABs: The absorption of dislocations due to continuous deformation results in an increase in misorientation, resulting in the formation of HABs. Moreover, the high dislocation density of LABs results in a migration to reach a more stable state.

- Migration of HABs: Large-curvature GBs may result in the migration of HABs, leading to a decrease in the corresponding areas of HABs and LABs. Further, subgrain coalescence may occur due to the rotation of subgrains, which finally forms recrystallized grains with HABs (Doherty and Szpunar, 1984).
- Change in the matrix topology: With the increase in strain, matrix deformation occurs, resulting in elongated matrix grains (Tu et al., 2019).

Here, LABs are GBs with misorientation angles less than 15°. Generally, LABs are composed of an array of dislocations and their properties and structure are a function of the misorientation (Gottstein, 2004). Moreover, subgrains are defined by the grains surrounded by LABs. When the misorientation angles of GBs are greater than 15°, the subgrains are considered to be recrystallized grains with HABs.

In this study, to simplify the analysis, the following assumptions were proposed: (1) dislocations are homogeneously distributed within the (sub)grains; (2) (sub)grains with a nearly ideal spherical shape are obtained, and the equivalent average radius of a (sub)grain is calculated by $r_i = (3N_iV_{cel}/4\pi)^{1/3}$, where N_i is the total number of cells belonging to a (sub)grain, and V_{cel} is the volume of each cell (Ding and Guo, 2001; Chen et al., 2021); (3) the mobility of LABs and HABs is primarily dependent on misorientation and temperature, while the mobility of LABs is significantly lower than that of HABs (Jägle and Mittemeijer, 2012); (4) the formation of subgrains commence after reaching a threshold value in dislocation density.

In summary, the mechanisms involved in the developed cDRX model include the formation of LABs due to the dislocation motion and reaction, rotation and migration of LABs, and migration of HABs/recrystallized grains. All these processes may be subject to mutual interference, thereby influencing the microstructural evolution during the hot-plastic forming process of the materials with high SFE.

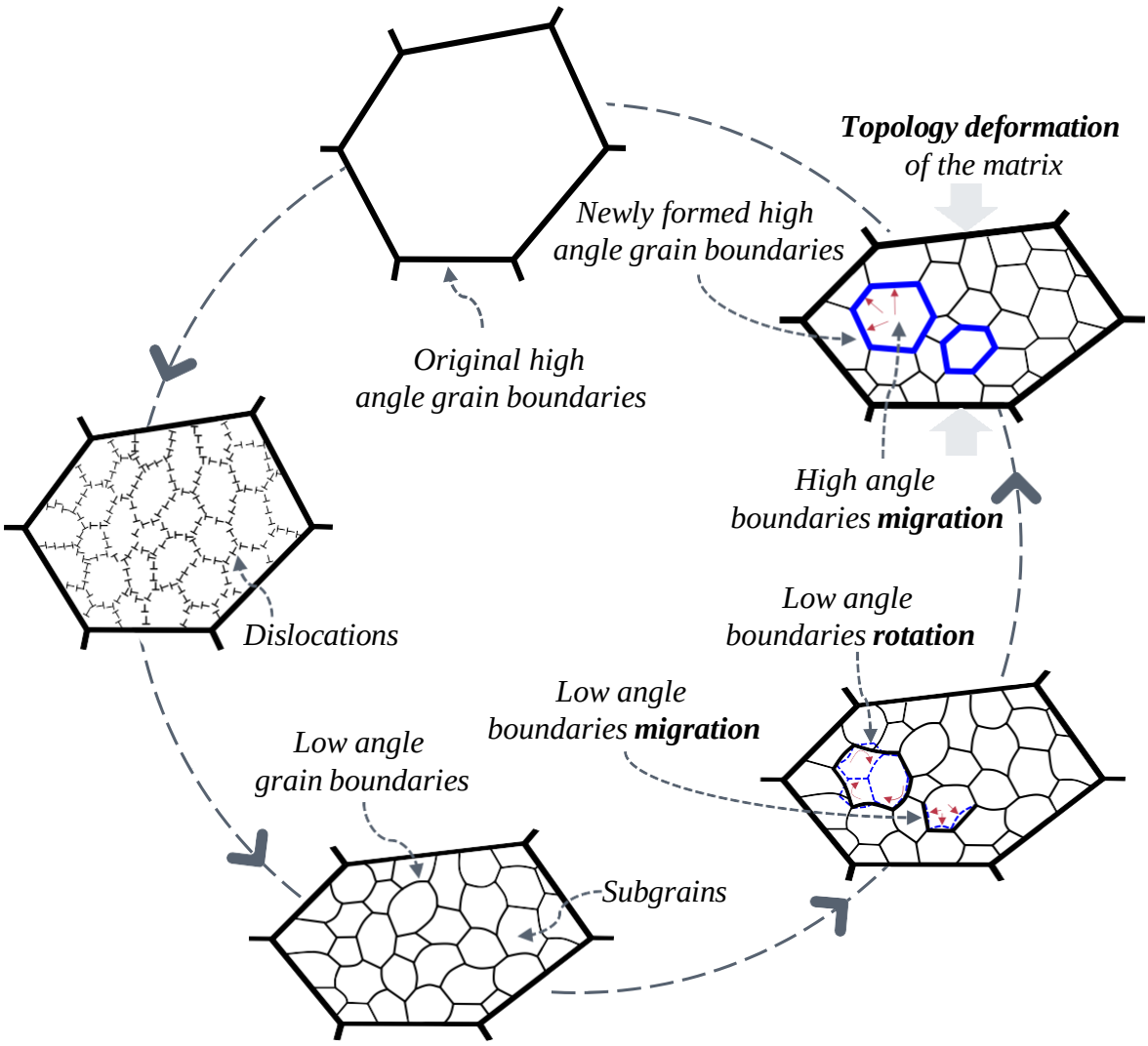

Fig. 1. Schematic of the microstructural evolution characterized with cDRX

In practice, the dominant mechanism may change from cDRX to dDRX and gDRX, or co-existence of three types of recrystallization mechanisms under different deformation conditions (Huang and Logé, 2016). In this study, the microstructural evolution of AA7075 aluminum alloy was mainly governed by cDRX within the investigated temperature and strain ranges. Therefore, the proposed model only considers cDRX mechanism.

Additionally, it should be noted that the secondary recrystallization is not taken into full account in the developed MCA-cDRX model. This is because, on the one hand even at very large strains the original microstructure is hard to be completely replaced by the new subgrain structure in cDRX. On the other hand, the development of microshear bands (MSBs) or kinking bands is easily inhibited under certain grain orientations conditions (Sakai et al., 2014).

2.2. Dislocation density evolution model

During hot deformation of aluminum alloys, the dislocation density is mainly composed of three contributions: (1) the formation of dislocation cells and subgrains hinders dislocation migration and facilitates the multiplication of dislocation; (2) DRV results in the

rearrangement and elimination of the dislocation through climbing and cross-slip mechanisms; (3) the migration of HABs is accompanied by the absorption of lattice dislocation. By considering these three contributions to dislocation evolution, the dislocation density ρ_i in the i^{th} subgrain/cell, which is uniform for all subgrains, was calculated using an extended GM model as follows:

$$\frac{d\rho_{i(\tilde{\varepsilon})}}{d\tilde{\varepsilon}} = \rho_i^{1+}(\tilde{\varepsilon}) - \rho_i^{2-}(\tilde{\varepsilon}) - \rho_i^{3-}(\tilde{\varepsilon}) \quad (1)$$

$$\frac{d\rho_{i(\tilde{\varepsilon})}}{d\tilde{\varepsilon}} = c_{1\sqrt{\rho_{i(\tilde{\varepsilon})}}} - c_2\left(\dot{\tilde{\varepsilon}}, T, Q_{act}\right)\rho_i(\tilde{\varepsilon}) - \frac{c_3\rho_i(\tilde{\varepsilon})s_{HAB}(\tilde{\varepsilon})v_{HAB}(\tilde{\varepsilon})}{\dot{\tilde{\varepsilon}}} \quad (2)$$

where $\tilde{\varepsilon}$ is the effective strain, is the effective strain-rate, T is the deformation temperature, s_{HAB} is the area of the HAB, c_1 and c_3 are material constants, and $c_2(\dot{\tilde{\varepsilon}},T,Q_{act})$ is a function of the strain rate, deformation temperature, and activation energy (Estrin, 1998), which is formulated as follows:

$$c_2(\dot{\tilde{\varepsilon}},T,Q_{act}) = c_{20}\left[\dot{\tilde{\varepsilon}}\exp\left(\frac{Q_{act}}{RT}\right)\right]^{-\xi} \quad (3)$$

where c_{20} and ξ are material constants, and R is the gas constant.

v_{HAB} is the GB migration rate of HABs, which can be expressed as

$$v_{HAB} = m_{HAB}p_{HAB} \quad (4)$$

where m_{HAB} and p_{HAB} indicate the mobility of the GB and driving force for GB movement per unit area, respectively, which are calculated as

$$p_{HAB} = \tau\left[\rho_{matrix} - \rho_i(\tilde{\varepsilon})\right] - \frac{2\gamma_\beta}{r_i} \quad (5)$$

where τ is the dislocation line energy, ρ_{matrix} is the dislocation density of the matrix, γ_β is the GB energy per unit area, and r_i is the equivalent radius of a (sub)grain with HABs. γ_β is calculated by the modified Ready-Shockley equation (Mallick and Vedantam, 2009):

$$\gamma_\beta = \frac{\mu_0 b\theta_m}{4\pi(1-\nu)}\sin(2\theta_i)\{1 - r_i ln[\sin(2\theta_i)]\} \quad (6)$$

where θ_i is the misorientation, θ_m is the misorientation for HABs, and ν is the Poisson's ratio.

$$m_{HAB} = \frac{b\delta D_{ob}}{k_B T} \exp\left(-\frac{Q_b}{RT}\right)$$

(7)

where b is the Burgers vector, δ is the GB thickness, D_{ob} is the GB self-diffusion coefficient, k_B is Boltzmann constant, and Q_b is the GB diffusion activation energy.

2.3. Critical condition for subgrain formation

According to the microstructure features in cDRX that were observed by Beer and Barnett (2007), Musin et al. (2010), Sun et al. (2014), and Gupta et al. (2019), it can be clearly observed that GB bulging occurs simultaneously in both the subgrain and the pre-existing HABs. This perspective has recently gathered strength, which can be referred to in the superior review work presented by Sakai et al. (2014) and Huang and Logé (2016). Moreover, a typical characteristic of dDRX called necklace microstructure can also be observed in cDRX. Therefore, without a loss of generality, the onset of subgrain formation is assumed to be associated with the bulging mechanism of GBs owing to the accumulation of dislocations. When the dislocation density of a deformed matrix reaches a critical value, called the threshold energy of cDRX, subgrain formation may occur. Here, the analogous critical dislocation density, $\rho_{critial}$, can be calculated using the following equation (Robers and Ahlblom, 1978):

$$\rho_{critical} = \left(\frac{20\gamma_\beta \dot{\tilde{\varepsilon}}}{3blm_{HAB}\tau^2}\right)^{1/3}$$

(8)

where γ_β is the GB energy per unit area, l is the average mean free path of the mobile dislocation, which can be calculated as $l = 20/\sqrt{\rho_0}$ (Takaki et al., 2014), and τ is the dislocation line energy, which is expressed as $\tau = \mu_0 b^2/2$.

Based on the nucleation model for recrystallization with a characteristic known as the strain- induced boundary migration and the concept of incorporating the nucleation from cube bands and GB regions together, a straightforward model to describe the distribution rules of subgrain size across the GBs has been developed as follows (Vatne et al.,1996):

$$N_{sub} = p\lambda \frac{S_V}{\delta_{sub}^2} \tag{9}$$

where p is the probability of identifying a subgrain with a size larger than a critical value that can provide the nucleus for recrystallization, λ is the geometric parameter, δ_{sub} is the average subgrain size, and S_V is the surface area per unit volume, which is calculated approximately as $S_V = [0.429\exp(-\tilde{\varepsilon}/1.155) + \exp(\tilde{\varepsilon}/1.155) + 0.571] \cdot d_{ini}^{-1}$ for aluminum (Sellars and Zhu, 2000).

To simplify the model, the dislocation density in each subgrains returns to the initial value, ρ_0 , which is set to 10^{10}m^{-2}, when subgrain formation occurs. The dislocation density increases significantly in a very short time according to Eq. (1). Meanwhile, it evolves differently from the matrix and the newly recrystallized grains.

As shown in Fig.1, it is noted that the formation of subgrain boundaries primarily originates from the dislocation cell substructures due to the dislocation motion and reaction. However, the geometric scale of dislocation is far less than the minimum simulation accuracy of MCA. In other words, the formation of dislocation cell substructures is far beyond what MCA can describe. Therefore, in the proposed MCA-cDRX model, the simulation of work hardening and dynamic recovery is approximately realized in terms of using the phenomenological dislocation density evolution model (Eq.1) and subgrain nucleation model (Eq.9).

2.4. Misorientation evolution model during subgrain rotation

During hot deformation, the formation of new subgrains via DRV process is characterized by a low initial misorientation angle of approximately 0.5°-1.5° (Humphryeys and Hatherly, 2004; Huang and Logé, 2016; Chen et al., 2020). Instead of the nucleation and growth mechanism of dDRX, the transformation of the new LABs of subgrains into HABs is dominated by the rotation by the absorption of dislocations. Further, it is commonly recognized that the transformation generally occurs at elevated temperatures, which can promote dislocation climbing and gliding mechanisms (Prangnell and Bate, 2007).

Governed by the mechanism of subgrain rotation, the misorientation angle of the subgrain boundaries gradually increases to the critical angle corresponding to HABs. Thus, it is necessary to quantify the relationship between the misorientation angle and dislocation density.

For LABs, a phenomenological geometric model was developed as follows (Humphreys and Hatherly, 2004; Winning et al., 2010):

$$\theta_i = \frac{b}{D} = b\sqrt{\tilde{\rho}_i(\tilde{\varepsilon})} \tag{10}$$

where b is the Burgers vector, and D is the spacing distance between two neighboring dislocations, which can be calculated as $1/\sqrt{\tilde{\rho}_i(\tilde{\varepsilon})}$ (Sun et al., 2018; Chen et al., 2020). Here, $\mathrm{d}\tilde{\rho}_i(\tilde{\varepsilon})$ represents the assimilation of dislocations by subgrain boundaries, which is defined as $\beta_1\left[\dot{\tilde{\varepsilon}}\exp\left(-\frac{Q_{act}}{RT}\right)\right]^{-\chi_1}\tilde{\rho}_i(\tilde{\varepsilon})\mathrm{d}\tilde{\varepsilon}$. Then, the change of misorientation of subgrains is obtained as follows:

$$\frac{\mathrm{d}\theta_i}{\mathrm{d}\tilde{\varepsilon}} = \frac{1}{2}\beta_1 b\left[\dot{\tilde{\varepsilon}}\exp\left(-\frac{Q_{act}}{RT}\right)\right]^{-\chi_1}\sqrt{\tilde{\rho}_i(\tilde{\varepsilon})} \tag{11}$$

According to Eq. (11), the evolution of misorientation angle only depends on amounts of absorbed dislocations, strain rate, and deformation temperature. However, as stated by Doherty et al. (1997), Moldovan et al. (2002), Chen et al. (2020), and Borodin et al. (2020), the rate and amount of subgrain rotation are also determined by the subgrain size, subgrain misorientation, initial grain size and stored energy.

Considering these mechanisms that govern the evolution of subgrains, a modified expression was established to calculate the change in the misorientation of the subgrain as follows:

$$\frac{\mathrm{d}\theta_i}{\mathrm{d}\tilde{\varepsilon}} = \frac{1}{2}\beta_1 b\sqrt{\tilde{\rho}_i(\tilde{\varepsilon})}\left[\dot{\tilde{\varepsilon}}\exp\left(-\frac{Q_{act}}{RT}\right)\right]^{-\chi_1}\left(\frac{d_{ini}}{d_{avr}}\right)^{1/3}(E_{sub})^{\lambda_1} \tag{12}$$

where d_{ini} is the initial diameters of the matrix, d_{avr} is the average diameter of all the grains, λ_1 is the material constant, and E_{sub} is the stored energy of the subgrain boundary, which was expressed as follows (Sellars and Zhu, 2000):

$$E_{sub} = \frac{\mu_0 \exp\ -K_g T\ \ b^2}{10}\left\{\rho_i(\tilde{\varepsilon})(1-\ln(10b\sqrt{\rho_i(\tilde{\varepsilon})})) + \frac{S_{sub}\theta_i}{b}\left(1+\ln\left(\frac{\theta_m}{\theta_i}\right)\right)\right\} \tag{13}$$

where S_{sub} is the area of the subgrain boundary, and θ_m is the critical misorientation for HABs. The classical relationship $S_{sub} = 2/\delta_{sub}$ can be employed, where δ_{sub} is the subgrain size.

2.5. Grain growth model for subgrain migration

Deformation results in the concentration of dislocations, which may subsequently form the subgrains with LABs. Then, the continuous absorption of dislocations into the subgrain boundaries leads to the occurrence of subgrain rotation recrystallization (Cho et al., 2019). Moreover, the growth of newly formed subgrains can be promoted by thermal assistance (Siu et al., 2011). Therefore, the modeling of the migration of subgrain boundaries until they are transformed into HABs, performs a key role in describing the cDRX during the hot deformation of aluminum alloy.

As mentioned by Humphreys and Hatherly (2004), the migration rate of LABs (v_{sub}) can be calculated using Eq. (4), $v_{sub} = m_{sub}p_{sub}$, where m_{sub} and p_{sub} are the GB mobility and driving force per unit area on the LABs, respectively.

In cDRX, the mobility of the subgrain boundary in LABs increases with the misorientation, until the critical condition (Θ_m=15°) is reached; then, m_{sub} is no longer dependent on misorientation (Huang and Humphreys, 2000; Humphreys and Hatherly, 2004). Therefore, m_{sub} can be expressed as

$$m_{sub} = \beta_2 \left(\frac{\theta_i}{\theta_m} \right)^{\chi_2} \exp\left(-\frac{Q_b}{RT} \right) \tag{14}$$

where β_2 and χ_2 are material constants.

Without considering precipitation and second-phase particles, the primary driving force for the migration of LABs originates from the surface energy reduction of subgrains. Based on the assumed conditions, the spherical subgrain shape and uniform distribution of driving force on the subgrain surface, p_{sub} , can be expressed as

$$p_{sub} = \left[\left(\frac{\theta_i}{\theta_m} \right) \left(1 - \ln\left(\frac{\theta_i}{\theta_m} \right) \right) \right] \rho_i(\tilde{\varepsilon}) \mu_0 \exp(-K_g T) b^2 \tag{15}$$

where μ_0 is the shear modulus, and K_g is the material constant.

3. MCA-cDRX modeling

The MCA-cDRX model for 7075 aluminum alloy was established based on the physical and mechanical metallurgy of cDRX. Figure 2 shows the basic integration scheme as an example for the application of MCA. The specific implementation of MCA-cDRX model consists of the following modules.

3.1. The basic components of the developed MCA model

- The cube was used as the cell;
- 3D von Neumann neighborhood was used, which means only considering the effect of state variables change of the closest six cells on the centre cell;
- The initial cellular space was set as 50×50×50, corresponding to the computation volume of 100×100×100 μm^3 in the real deformed material. To avoid losing neighbors of the cell on the border of 3D cellular space, periodic boundary conditions (PBCs) were used to represent approximately infinite space.
- Each cell has seven state variables: the dislocation density variable, the grain orientation variable, the grain boundary variable, the recrystallized fraction variable, the subgrain size variable, grain number variable, and grain type variable. The physical meaning of the first six state variables can be referred to Appendix A1 in our previous work (Chen et al., 2021). The last one was used to determine if the cell belongs to matrix or subgrain.
- The established state switching rules were introduced in detail in Sections 3.4 and 3.5.

3.2. Initial microstructure generation module

During the hot working of aluminum alloy, the initial microstructure can be obtained by electron backscatter diffraction (Tu et al., 2019). Owing to the complex heating process for the blooming of aluminum ingots, the casting dendrites are usually replaced by microstructures that are characterized by equiaxed grains, elongated matrix, and local fine subgrains. The basic idea of the formation of the initial microstructures is as follows.

- The initial equiaxed grains are generated using the cube cell. Based on the basic physical metallurgical principles, such as the thermodynamic driving mechanism, curvature driving mechanism, and lowest energy principle, cellular state switching rules are established to generate the initial equiaxed microstructure (refer to Appendix A1).
- Based on the experimental data obtained by Sakai et al. (2014) and Li et al. (2020), the initial microstructure before the hot-forming process (e.g., hot forging, hot rolling, and hot extrusion) is frequently constructed by the elongated grains. To obtain the elongated grains, a topology deformation technique (Chen et al., 2010) was adopted and further extended to 3D space. The details of this method are concisely introduced in Appendix A2.
- Based on the initial microstructures obtained by Sun et al. (2018), it is obvious that several fine subgrains exist in some of the elongated grains. The distribution function of the misorientation angle of LABs can be obtained using a nonlinear regression method. In MCA, all the previously elongated grains are initially renumbered, and some of them are selected; then, the orientations of all the cube cells within the selected grains are randomly reset to an angle less than 15°. Furthermore, the cube cells may grow based on the cellular state switching rules to construct the initial microstructures with an elongated matrix and fine subgrains.

3.3. Work hardening and dynamic recovery module

During the hot-working process of aluminum alloys, an external energy is applied to the material. The number of dislocations is often used to quantify the work hardening process. Moreover, the energy is almost always added at a sufficiently fast speed and large amount, which can not only move existing dislocations but also generate a large number of new dislocations through the fully deformed material. New dislocations are produced in proximity to a Frank-Read source (Smith et al., 2020). Additionally, the DRV of the aluminum alloy is usually characterized by the elongation of the matrix grains and formation of dislocation cell and substructures before critical strain.

However, the geometric scale of the generation and interaction of dislocations is considerably less than the minimum simulation accuracy of CA simulation. Therefore, the simulation of the dislocation evolution behavior is primarily based on the phenomenological formation of initial substructures, which includes subgrain nucleation and subgrain growth.

The critical condition for subgrain nucleation is that the dislocation density of the deformed matrix, which is calculated according to Eq. (2), reaches the critical value calculated by Eq. (8). Then, the number of subgrain nuclei is calculated based on Eq. (9). The

growth of the subgrain nuclei is discussed subsequently. They grow isotropically and freely according to the established switching rules. When the size of the subgrain reaches the initial stable subgrain size, the individual growth of the subgrain nuclei is terminated.

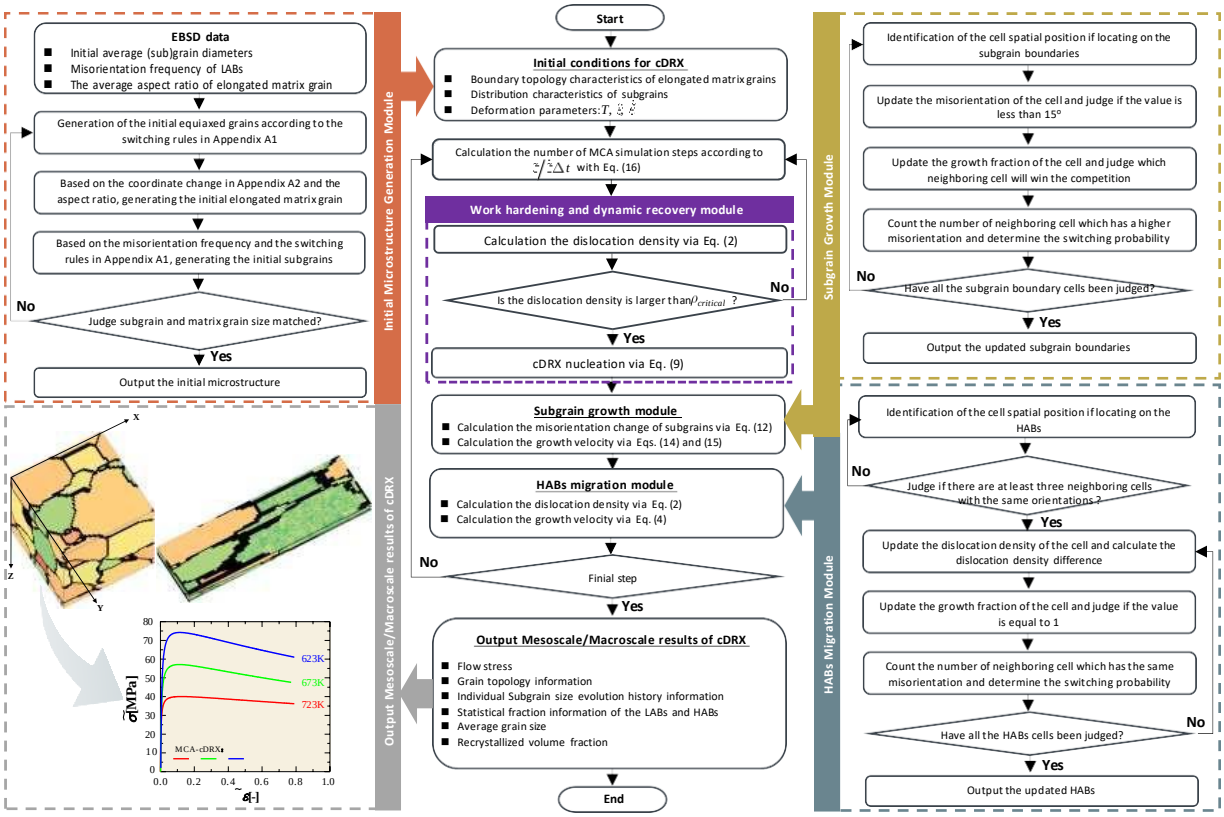

Fig.2. Flowchart of the MCA modeling of cDRX

3.4. Subgrain growth module

In the MCA simulation of cDRX, the time step Δt is defined as the ratio of the cell diameter to the maximum GB velocity, $v_{\max}$, which is calculated as follows:

$$\Delta t = \frac{d_0}{v_{\max}} = \frac{d_0}{\rho_i(\tilde{\varepsilon})\mu_0 b^2 \beta_2 \exp\left(-K_g T - \frac{Q_b}{RT}\right)} \tag{16}$$

where d_0 is the initial size of the cell. Then, the strain increment is expressed as $\Delta\varepsilon = \dot{\varepsilon}\Delta t$. At each time step, the dislocation density and misorientation of all subgrains were updated based on Eq. (1) and (12), respectively. Then, the subgrain boundary migration distance at time *t* is calculated as $\varsigma^t = \varsigma^{t-\Delta t} + v_{sub}\Delta t$.

The switching rules that control the state change of cells during subgrain growth were established as follows: (1) The misorientation of the cell is less than 15°. (2) The cell is located at the subgrain boundaries. (3) If more than one neighboring subgrain boundary cell consumes the same cell within a time step, the grain growth fraction variable calculated by $f^t = (\varsigma^{t-\Delta t} + v_{sub}\Delta t)/l_i$ is individually evaluated and then compared. Consequently, the cell that first satisfies the condition of $f^t = 1$ will win the competition. (4) It is commonly known that the most significant feature of a CA model is the probability control method (Raabe D., 1999; 2002). In this study, the state transformation probability only depends on the number ϖ_i of von Neumann neighboring cells, which have a larger misorientation when compared with that of the cell waiting for state transformation. If $M_i/100$ (M_i is a random number generated from 0 to 100) is less than $P_i = \varpi_i/6$, then state transformation occurs.

3.5. HABs migration module

As emphasized by Fan and Yang (2011) and Chen et al. (2020), there are two types of HABs: mobile and immobile. In this study, the GBs of the initial elongated matrix were recognized as immobile HABs. For this type, only the topological morphology changes with the increase in strain. The GBs of the newly recrystallized grains that originate from the rotation and migration of subgrains are considered as mobile HABs. However, mobile HABs may be immobilized during cDRX owing to the balance of the dislocation density. Thus, the difference in the dislocation density between the matrix and recrystallized grains provides the driving force for HAB migration. Conversely, the GB curvature may also drive the migration of HABs (Beucia et al., 2018). By combining the above two aspects, the control state switching rules are established as follows: (1) A cell is located at the GB, and simultaneously, there are at least three cells in its von Neumann neighbourhood that have the same orientations. This rule implies that the curvature-driven mechanism dominates the migration of HABs. (2) The HAB cells were selected and local radius was obtained as

$r_i = (3N_iV_{cel}/4\pi)^{1/3}$; moreover, the growth velocity, driving pressure, and GB energy were calculated using Eq. (4), (5), and (6), respectively. The grain growth fraction variable, which was calculated as $f^t = \varsigma^{t-\Delta t} + v_{HAB}\Delta t/l_i$, is equal to 1. (3) The state transformation probability of the cell was calculated as $P_i = \varpi_i/6$. ϖ_i is the number of cells that have the same orientations in its von Neumann neighborhood.

4. Results and discussion

To validate the model, simulations were conducted, and the simulation data were compared with the results of the experimental study on the cDRX behavior and plastic flow of AA7075 alloy under the isothermal hot compression as reported by Sun et al. (2018). The material parameters used in the simulations are listed in Table 1. Generally, the materials parameters can be divided into the following three basic categories:

- Material constants. For example, the shear modulus (μ_0) and Burgers vector (b) of the studied alloy, Boltzmann constant (k_B), Poisson's ratio (υ), and gas constant (R) are constants for different kinds of materials.
- Physical quantitates. For example, the activation energy (Q_{act}), the GB diffusion activation energy (Q_b) can be referred to the classic literature. Additionally, molecular dynamics (MD) can be also employed to calculate these parameters.
- Fitting parameters. For example, the parameters (c_1 ,c_{20} andc_3 , etc.) of the dislocation density model can be calculated using GA-based objective optimization technique (Sun et al., 2018).

When the developed MCA-cDRX is used to simulate the microstructure evolution for other materials characterized with high SFE. All the regression parameters should be calculated based on the flow stress data.

Table 1

Material parameters for AA7075 alloy [3].

Material constants			**Physical quantities**			
μ_0	b	k_B	Q_{act}	Q_b	δD_{ob}	K_g
(Pa)	(-)	(J/K)	(kJ/mol)	(kJ/mol)	(m^2/s)	(1/K)
2.99×10^{10}	2.86×10^{-10}	1.38×10^{-23}	177.5	70	2.4×10^{-15}	5.4×10^{-4}
Fitting parameters						
c_1	c_3	c_{20}	β_1	β_2	χ_1	χ_2
(−)	(−)	(−)	(−)	(m^4/Js)	(-)	(-)
2.8×10^{8}	1.0×10^{11}	1.5×10^{3}	2.37×10^{8}	3×10^{-6}	0.485	5.18
Fitting parameters						
λ	λ_1	p	ξ			
(-)	(−)	(-)	(−)			

[3] c_1, c_{20}, c_3, β_1, χ_1, δD_{ob}, ξ, λ_1 and Q_{act} (Sun et al., 2018); p and λ (Sellars and Zhu, 2000); Q_b, K_g, χ_2 and β_2 (Huang and Humphreys, 2000); k_B, μ_0 and b (Duan and Sheppard, 2002).

0.29	0.1	0.021	0.095

4.1. Initial microstructures before hot-working

Based on the experimental data from Sun et al. (2018), which were analyzed by Chen et al. (2020), the initial sizes of the matrix and subgrain were set as 68 μm and 8 μm, respectively. In this study, the initial equiaxed grains were first constructed by the initial microstructure generation module, as shown in Fig. 3(a). Usually, the initial microstructures for hot compression are deformed by blooming technologies such as extrusion (Aukrust et al., 1997) and rolling (Khan and Baig, 2011). Coupling of the elongated matrix with the subgrains is inevitably induced (Sakai et al., 2014; Sun et al., 2018; Nayan, et al., 2019; Tu et al., 2019). From the experimental data (Sun et al., 2018), the average ratio ϑ of the grain thickness to length is approximately equal to 0.3076 [4]. According to the relation ($\tilde{\varepsilon} = 2\ln \vartheta/3$), the initial elongated grains were generated by using the topology deformation technique illustrated in Fig. A2-T (refer to Appendix A2-T), as shown in Fig. 3(b1). Thus, the formation of the initial elongated grains coupled with local subgrains is constructed and shown in Fig. 3(c1). Based on the misorientation angle frequency distribution as shown in Fig. 3(c2), it was determined that the distribution trend is similar to that in the experimental data. The LAB fraction and average misorientation angle of the constructed initial microstructure are 82.61% and 8.22°, respectively, which are significantly close to the experimental results of 85.71% and 8.26°, respectively. Therefore, the initial MCA microstructures constructed in this study can be used for the following cDRX simulations.

[4] The values of grain thickness and length were calculated based on the statistical information from the experimental electron backscatter diffraction image using a commercial software named Image-Pro Plus 6®. Moreover, based on the distribution of the misorientation angles from the findings of experimental data, a probability function to determine the initial fraction of subgrain cells was established using a nonlinear exponential regression method, which is presented by $f_{inisub} = 1.2039 \times \exp\left(-\theta/0.9364\right) + 0.0151$, as shown in Fig. 3(d).

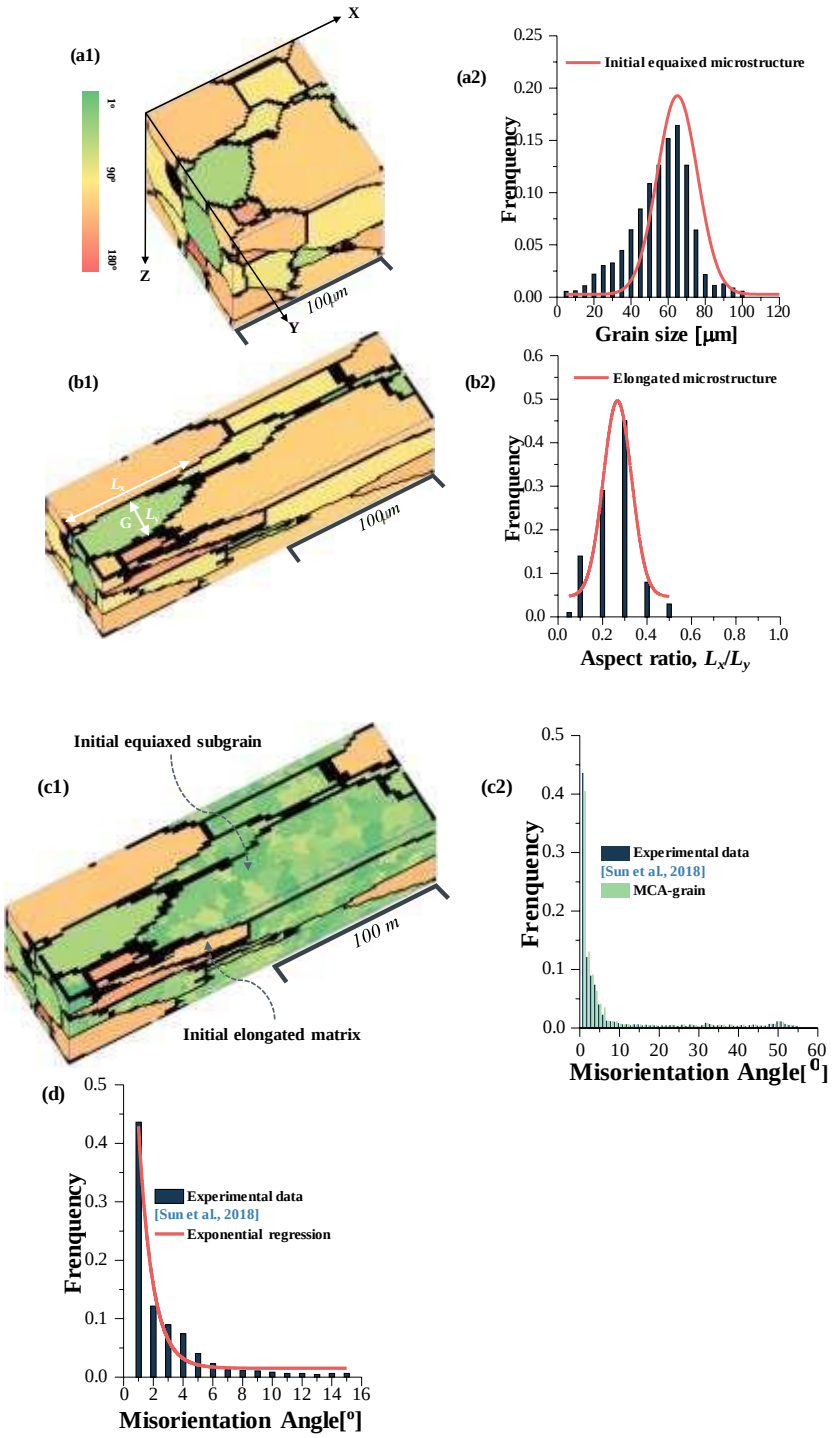

Fig.3. Initial microstructures for MCA simulation of cDRX. (a1) Equiaxed microstructure with matrix size of 68 μm, (a2) grain size distribution, (b1) elongated microstructure after extrusion cogging, (b2) aspect ratio L_y/L_x distribution, (c) exponential regression of the misorientation of LABs, (d1) initially coupled microstructures, and (d2) orientation distribution of misorientation angle

4.2. Features of the flow stress curves

As a bridge between the material flow and microstructure evolution, the prediction of flow stress is the cornerstone for understanding the plastic deformation behavior of materials. Therefore, the flow stress prediction accuracy of the developed MCA-cDRX model is of

considerable importance. The Taylor relation was employed, in which the flow stress is proportional to the square root of the average dislocation density as given in

$$\tilde{\sigma} = \mu b \sqrt{\bar{\rho}(\tilde{\varepsilon})} \tag{17}$$

where μ is the shear modulus calculated as $\mu(T) = 2.99 \times 10^4 \exp(-5.4 \times 10^{-4} T)$ (Duan and Sheppard, 2002) and $\bar{\rho}(\tilde{\varepsilon})$ is the average dislocation density of all cells. In the simulation, it can be calculated by

$$\bar{\rho}(\tilde{\varepsilon}) = \frac{1}{N_{totoal}} \sum_{i=1}^{N_{totoal}} \rho_i(\tilde{\varepsilon}) \tag{18}$$

where N_{totoal} is the total number of cells in the MCA model.

Figure 4 shows the flow stress data under different deformation conditions, i.e., at temperatures of 623, 673, and 723 K and strain rates of 0.01, 0.1, 1, and 10 s^{-1}, which are plotted using symbols. Moreover, the simulated data are plotted with lines in Fig. 4. Although there are still obvious deviations under the different temperature/strain rate deformation conditions of 623 K/0.01 s^{-1}, 673 K/0.01 s^{-1} and 623 K/0.1 s^{-1}, the simulated data show a good consistency with the experimental results. The root mean squared errors of the flow stress predictions under the above three deformation conditions are 3.22, 2.29 and 4.61 MPa, respectively, while the coefficient of determination of the flow stress predictions are 0.9712, 0.9915, and 0.9619, respectively. Moreover, it can be observed that the time taken to reach the peak stress in the simulations is marginally greater than that in the experiment. The marginal discrepancy is evident at the lowest temperature (623 K). This is because of the fine dispersion of second-phase particles caused by the instantaneous and significant increase in the deformation force at a relatively low temperature, which further hinders the migrations of LABs (Jazaeri and Humphreys, 2004). Conversely, the critical condition for the formation of new subgrains is based on an artificial hypothesis, which may also hinder the actual process of cDRX to a certain extent (Huang and Logé, 2016). Additionally, it is found that the differences of flow stress between the simulated data and experimental results become more apparent at the relatively low strain rates (0.01 and 0.1 s^{-1}), especially at the low temperature (623K) and the strain smaller than about 0.4. This may be due to the following reason: from the experiment data, it is clear that the flow stress rapidly drops at the true strain of about 0.05, which means the dDRX mechanism may be also triggered during hot deformation of AA7075 aluminum alloy. This phenomenon has been verified by the microstructure investigation of high purity aluminum by Yamagata et al. (2001) and AA 7085 aluminum alloy by Yang et al. (2016). Meanwhile, it is known that dDRX is strain rate dependent. Lower strain rate may promote the progress of dDRX (McQueen et al., 2004). But in this study, the softening due to the possible dDRX has not been considered because the cDRX mechanism still plays a dominant role in the softening of AA 7075 aluminum alloy (Sun et al.,

2018). Therefore, there is still large room to develop a more general DRX model in future study and research.

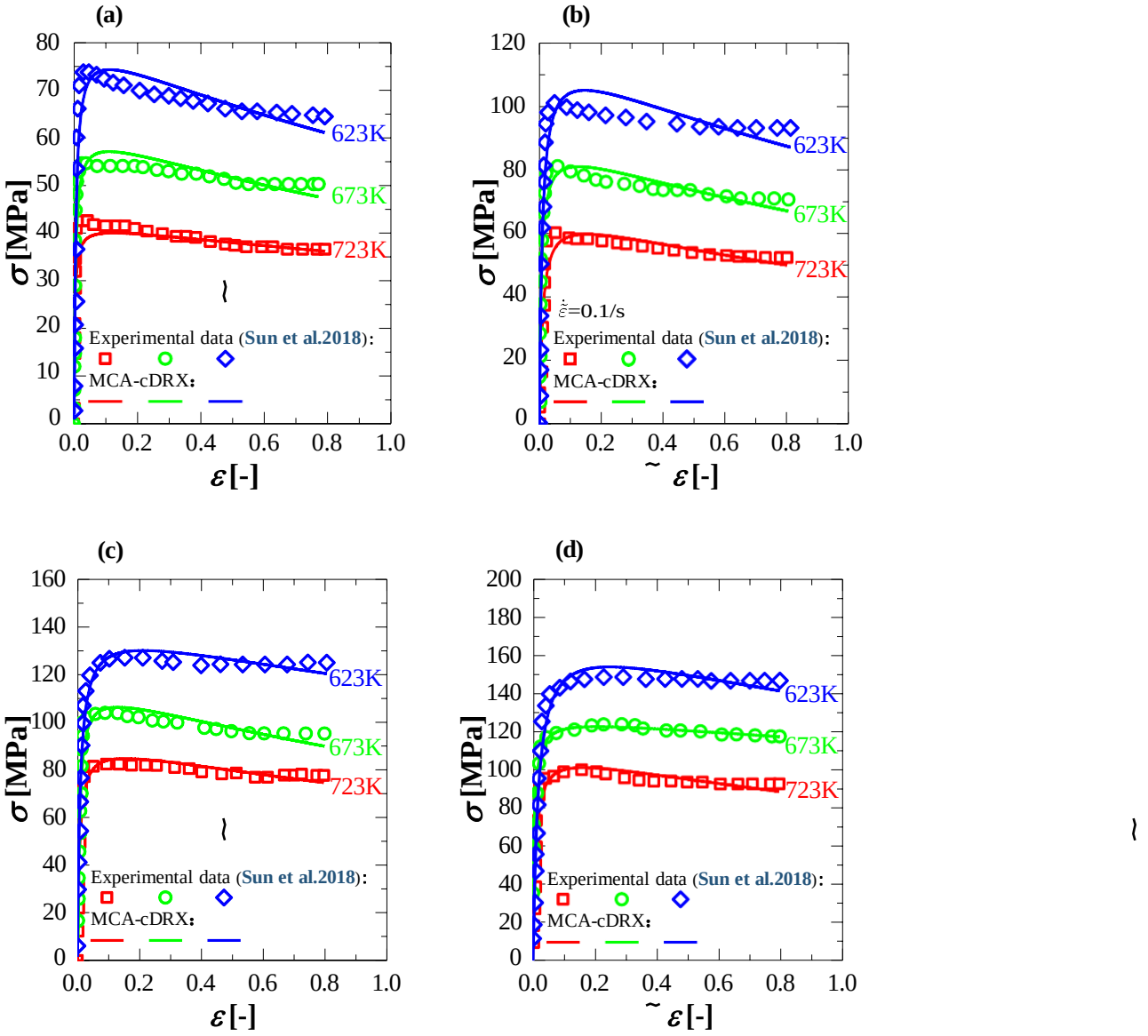

Fig.4. Comparisons between the true stress-strain curves obtained from the simulated data (lines) and experimental data (symbols) under different deformation conditions: (a) $\dot{\bar{\varepsilon}}$=0.01s^{-1}; (b) $\dot{\bar{\varepsilon}}$=0.1s^{-1}; (c) $\dot{\bar{\varepsilon}}$=1s^{-1} and $\dot{\bar{\varepsilon}}$=10s^{-1}.

4.3. Recrystallization kinetics

Recrystallization kinetics is commonly used to quantitatively describe the degree of recrystallization. Usually, there is an incubation period where the subgrains form, they begin to rotate and grow at a certain rate, and then they gradually consume the deformed matrix (Humphreys and Hatherly, 2004; Sakai et al., 2014).

To investigate the influence of different strain rates and temperatures on the kinetics, the recrystallized volume fractions under different deformation conditions were calculated, as shown in Fig. 5. From the figure, it is obvious that a higher degree of recrystallization

appears at a relatively low Zener-Hollomon parameter, $Z = \dot{\varepsilon}\exp(Q_{act}/RT)$. This tendency is consistent with the findings of the experiments. According to the simulations, the recrystallization kinetics of AA7075 alloy show the following characteristics: (1) the incubation period is significantly short, which implies that a considerably small fraction of time is required for the initiation of subgrain formation. In the tested Zener-Hollomon range, the critical strain for the initiation of recrystallization is less than 0.05. These factors result in the flow stress reaching a peak value rapidly, as shown in Fig. 4. (2) At the same strain rate, the recrystallized fraction dramatically increases with an increase in temperature from 623 to 723 K. This may be related to the fact that a higher temperature accelerates the accumulation of the dislocations of subgrains with LABs (<1-2°), and promotes the rotation of the subgrains corresponding to their neighbors (Doherty et al., 1997). (3) A similar trend can be also observed when the strain rate decreases from 10 to 0.01 s^{-1} at a constant temperature. This suggests that the DRV has displaced DRX as a dominant dynamic softening mechanism with an increase in the strain rates. (4) As shown in Fig. 5, at the strain rate of 10 s^{-1}, the recrystallized volume fraction is still less than 5% at a strain of 0.8. This indicates that the strengthening effect originating from LABs exceeds the limited strain softening caused by significantly small recrystallization fractions. Consequently, there is no obvious peak stress at the strain rate of 10 s^{-1} in Fig. 4.

Furthermore, the simulated values were compared with the experimental data and the results calculated using the cDRX-VPSC model (Chen et al., 2020). Experimentally, the deviations were 17.05%, 7.95% and 16.34 % under the deformation conditions of 723 K/10 s^{-1}, 723 K/1 s^{-1} and 723 K/0.1 s^{-1} at a strain of 0.7, respectively. Moreover, it was observed that a good agreement is also achieved between the MCA-cDRX and cDRX-VPSC predicted results, as shown in Fig. 5.

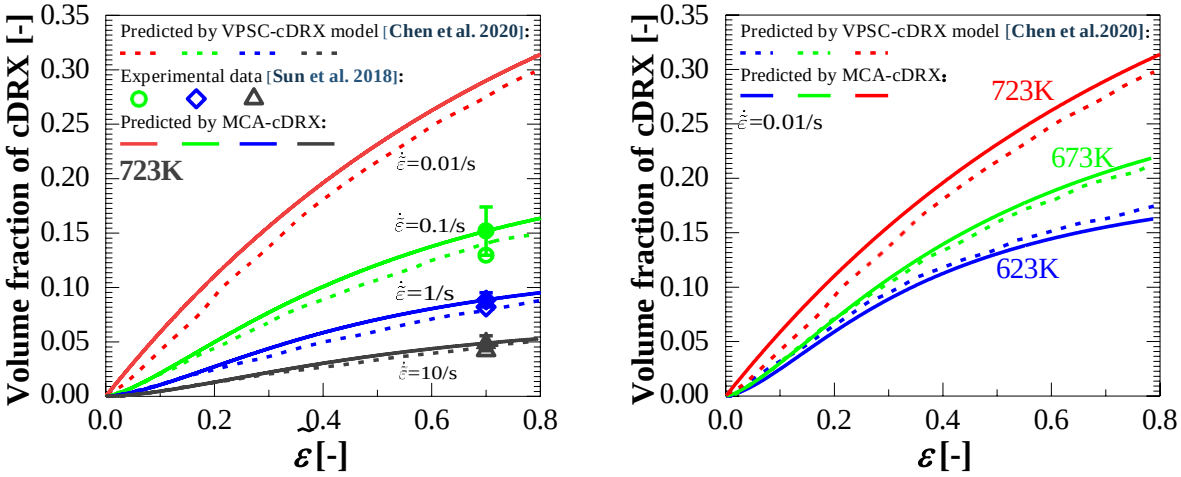

Fig. 5. Comparisons between the volume fraction calculated by MCA simulations (solid lines) and that obtained from the experimental data (symbols) reported by Sun et al. (2018) and cDRX-VPSC model simulations (dashed lines) proposed by Chen et al. (2020) at different deformation conditions

4.4. Features of subgrains

In the hot working of the aluminum alloy, subgrains are formed by the mutual annihilation of a large number of dislocations and the rearrangement of the remaining dislocations into regular LABs (McQueen, 2004). It was observed that the relatively rapid rates of cross-slip and climb mechanisms required for the above phenomenon exist only in metals and alloys with narrow dislocations, primarily because the high energy of their stacking faults inhibits the motion of dislocations. Finally, the low dislocation density contributes to a low flow stress and inhibits the formation of recrystallization nuclei during the hot working of the aluminum alloy.

In the MCA simulation, the formed subgrains were allocated with a unique number. The average subgrain size is calculated as $\langle \delta_{sub} \rangle = \sum_{i=1}^{N_{sub}} \delta_i \Big/ N_{sub}$. Figure 6 shows the evolution of the average subgrain size under different deformation conditions as the strain increases up to 1.2 (compression ratio equals to 70%). It shows that there is a sharp reduction in the subgrain size, when the strain is less than 0.2 under deformation conditions of 723 K/0.01 s^{-1}, 723 K/0.1 s^{-1}, 673 K/0.01 s^{-1} and 623 K/0.01 s^{-1}. Then, it increases gradually and nearly saturates to a constant value. Under these conditions, the evolution tendency of the subgrain is consistent with that observed in the study by Kaibyshev et al. (2005). As indicated by Chen et al. (2020), the slow migration of HABs may contribute to a marginal increase in the subgrain size. At the deformation conditions of 723 K/1 s^{-1}, 723 K/10 s^{-1}, the subgrain size decreased significantly and then reached a steady state, which agrees well with the experimental and simulated data (Sakai et al., 2014; Sun et al., 2018; Maizza et al., 2018; Chen et al., 2020).

Further, from Fig. 6, it can be observed that, when the deformation temperature (723K) is fixed, and strain rates are varied (0.01, 0.1, 1 and 10 s^{-1}), the simulated subgrain sizes are 6.48, 3.76, 2.44 and 1.89 µm, respectively. Conversely, when the strain rate (0.01 s^{-1}) is fixed, and temperatures are varied (673 and 623 K), the simulated results are 4.15 and 3.67 µm, respectively. The maximum deviation is 11.89%. The simulated subgrain sizes suitably agree with the experimental data.

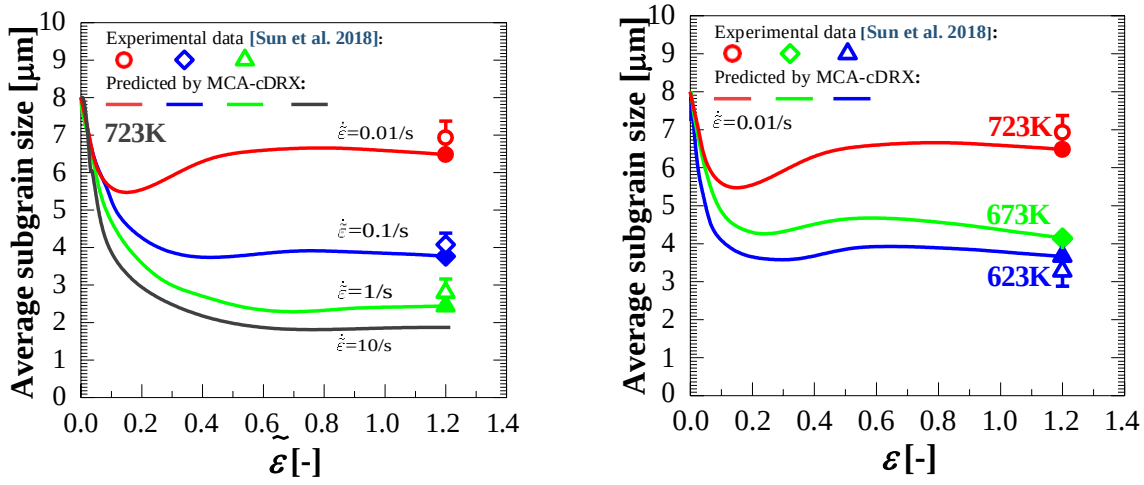

Fig. 6. Comparisons between the subgrain size obtained from the MCA simulations (solid lines) and experimental data (symbols) at different deformation conditions (true strain equals to 1.2)

Figure 7 depicts the simulated microstructures under different temperatures and strain rates when the strain is increased to 1.2. As shown in the figure, the subgrain size increases with increase in temperature and decreases with increase in strain rate. In the hot-deformation process, there are several dislocations that are predominantly stored in tangles/forests in the heavily deformed metal. In metals with low-to-medium SFE, it is difficult for the dislocation motion to occur, which commonly leads to a strong disorder in the distribution of dislocations. In contrast, it is easy to form cellular substructures in metals with moderate-to-high SFE (e.g., AA 7055 aluminum alloy), in which the rough tangles of dislocations are commonly observed in the cell walls.

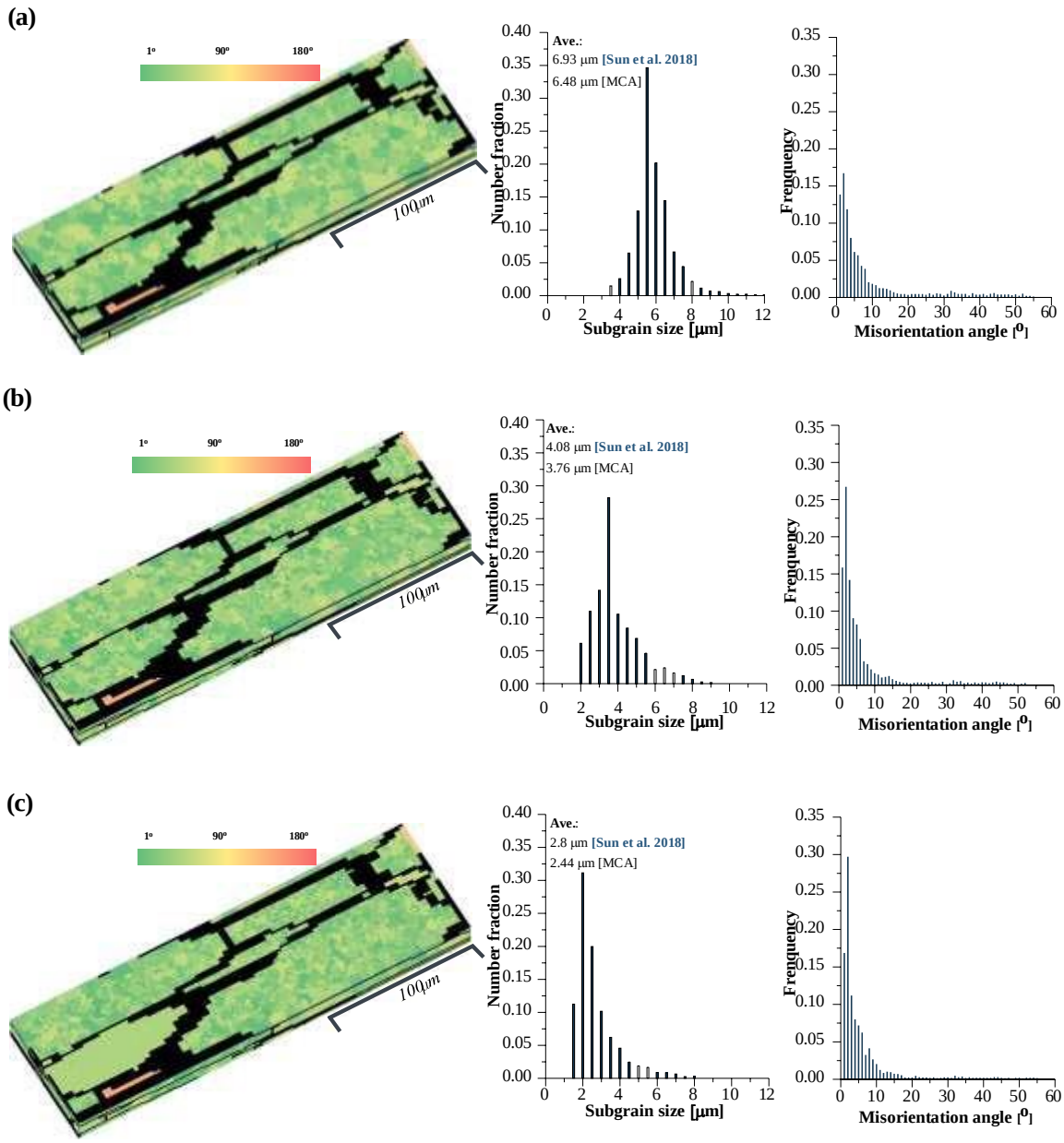

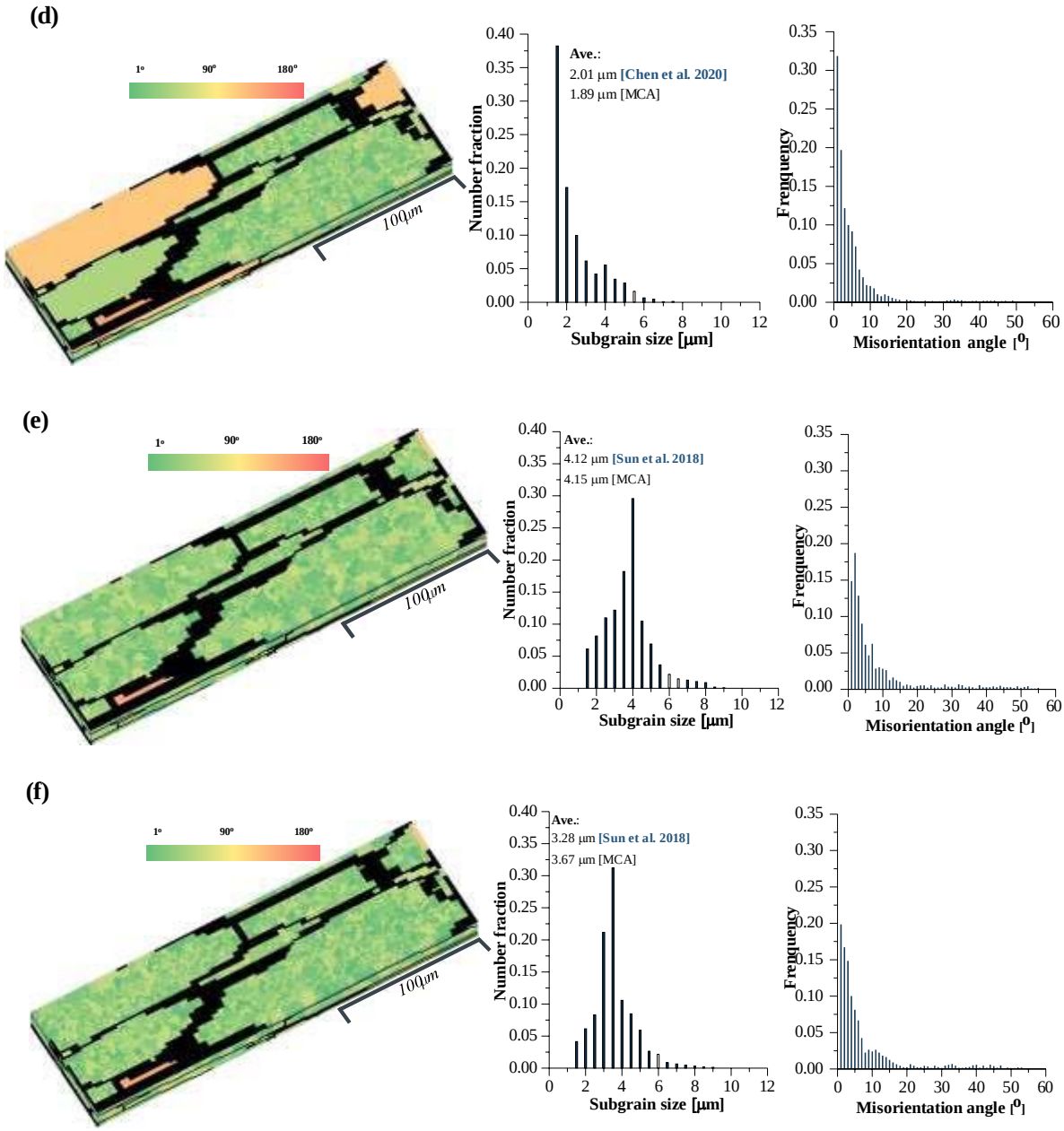

Fig. 7. Predicted microstructures of AA7055 aluminum alloy at 723K with a strain of 1.2 as generated by MCA simulations. Simulated results at different strain rates of (a) 0.01 s^{-1}, (b) 0.1 s^{-1}, (c) 1 s^{-1} and (d)10 s^{-1}. Simulated results at a strain rate of 0.01 s^{-1} and strain of 1.2 at different temperatures of (e) 673 K and (f) 623 K respectively

In the AA7055 aluminum alloy, the stored dislocations tend to align themselves into ordered arrays during DRV; then, dislocation walls (early version of LABs) are formed through both dislocation climb and cross-slip, which promote the formation of subgrains. At a relatively high temperature, the increase in atomic mobility significantly increases the dislocation climb and cross-slip and results in increased completion of the cancellation and recombination of dislocations, which finally enhances the subgrain growth in the aluminum alloy. Therefore, it can be observed that, with the increase in temperature, the subgrain size gradually increases. This indicates that higher temperature can promote larger subgrains formation and also motivates LAB migration and misorientation angle accumulation, which

accelerates the transformation of LABs into HABs. From Fig. 7(a), (e), and (f), it can be observed that the LAB volume fraction gradually decreases from 62.2 to 48.1% as the temperature increases gradually from 623 to 723 K. The average misorientation angle increases gradually from 13.4° to 18.6°. It can be concluded that the homogenization of misorientation distribution and the transformation of LABs to HABs were enhanced simultaneously as a result of the increasing temperature. The same trend can be observed when the strain rate decreases from 10 to 0.01 s^{-1} at 723 K. Thus, both the temperature and strain rate influence substructure evolution.

From Fig. 7, it is also observed that more fully polygonized subgrains are formed with increasing temperature and decreasing strain rate. The mechanism of polygonization predominantly relies on the propagation of subgrains and the arrangement of the subboundary dislocations into neater networks (Avramovic-Cingara et al., 1996; Sakai et al., 2014).

A relationship between the subgrain size and the Zener-Hollomon parameter is to be expected as the latter integrates the coupling effects of temperature and strain rate in the experiments. The unique relationship indicates that the thermo-activation mechanism dominates the cDRX process and the substructure primarily depends on the number of thermally activated events per unit strain, which is the reciprocal of the Zener-Hollomon parameter (Vatne et al., 1996; Donati et al., 2013).

In this work, to investigate the combined influence of temperature and strain rate on the subgrain size, a wide range of simulated data at various Zener-Hollomon parameters were plotted, as shown in Fig. 8(a). The relationship between the subgrain size and the deformation conditions can be quantitatively described by the following equation:

$$\delta_{sub}^{-1} = -0.68 + 0.07 \log Z \tag{19}$$

where

$$Z = \dot{\tilde{\varepsilon}} \exp(Q_{act} / RT) \tag{20}$$

where Z is a temperature compensated strain rate parameter (Zener-Hollomon parameter), and Q_{act} is the activation energy, which is 177.5 kJ/mol for AA7055 aluminum alloy (Sun et al., 2018).

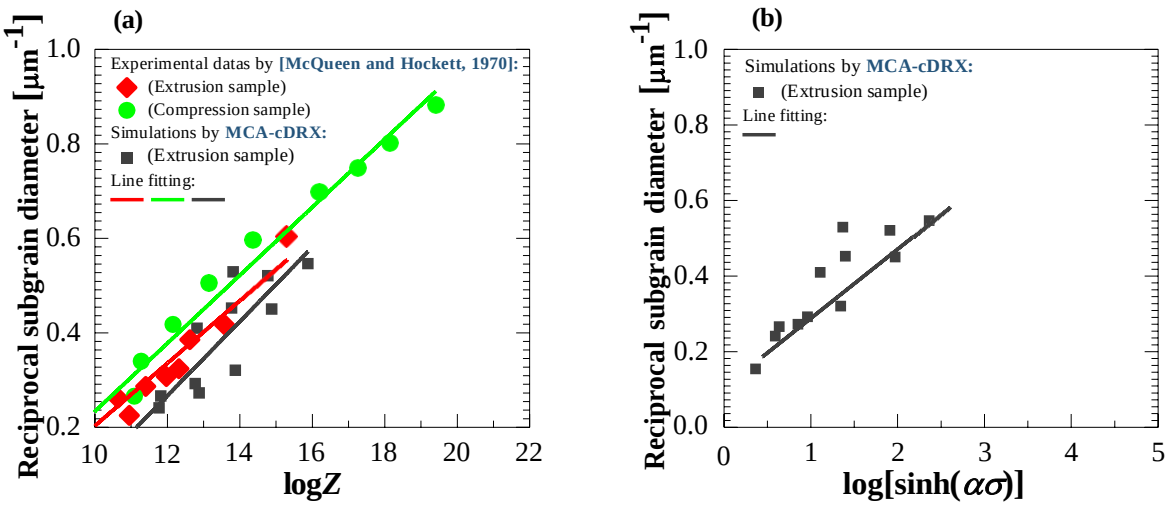

Fig. 8. (a) Relationship between the reciprocal subgrain size (δ_{sub}^{-1}) and logarithm of Zener-Hollomon parameter (Z). (b) Relationship between the reciprocal subgrain size (δ_{sub}^{-1}) and steady-state stress (σ_{ss}). Here, α equals to 3×10^{-4}(McQueen and Hockett, 1970)

Moreover, the relationship between δ_{sub}^{-1} and flow stress is of significant practical importance (Huang and Logé, 2016). Extracting the steady-state flow stress from the simulated data, which is shown in Fig. 4, the corresponding relationship between δ_{sub}^{-1} and the flow stress (steady-state value σ_{ss}) is plotted, as shown in Fig. 8(b), based on the equation, $\delta_{sub}^{-1} = 0.17 + 0.22\log\left[\sinh(\alpha\sigma_{ss})\right]$. According to the two relationships: $\delta_{avr}^{-1} \propto \log(Z)^{0.07}$ and $\delta_{avr}^{-1} \propto \log\left[\sinh(\alpha\sigma_{ss})\right]^{0.22}$, we obtain $Z \propto \left[\sinh(\alpha\sigma_{ss})\right]^{n}$. Accordingly, the value of n is 3.14, which is close to the findings in other studies on aluminum alloys (McQueen and Hockett, 1970; McQueen et al., 2010). Hence, the developed model can predict the average subgrain size together with the visible evolution of the subgrains at different Zener-Holomon parameter levels.

4. 5. Features of HABs

The evolution of HABs primarily depends on the following two contributions: the progressive annihilation of the original GBs and the generation of new HABs due to the increasing misorientation of the LABs (Gourdet and Montheillet, 2003). Figure 9 depicts the evolution of HAB volume fraction under different deformation conditions. It can be observed that both temperature and strain rate have an effect on the volume fraction of HABs. From the figure, it is obvious that the temperature has a significantly lower effect than the strain rate in the investigated range. At the same temperature, a lower strain rate results in a higher volume fraction of HABs, which agrees well with the experimental findings in the study on AA5052 (Gourdet, 1997) and simulations using AA7050 (Li et al., 2020). In other words, cDRX is more likely to occur at higher temperatures and lower strain rates. More newly recrystallized grains with HABs are formed.

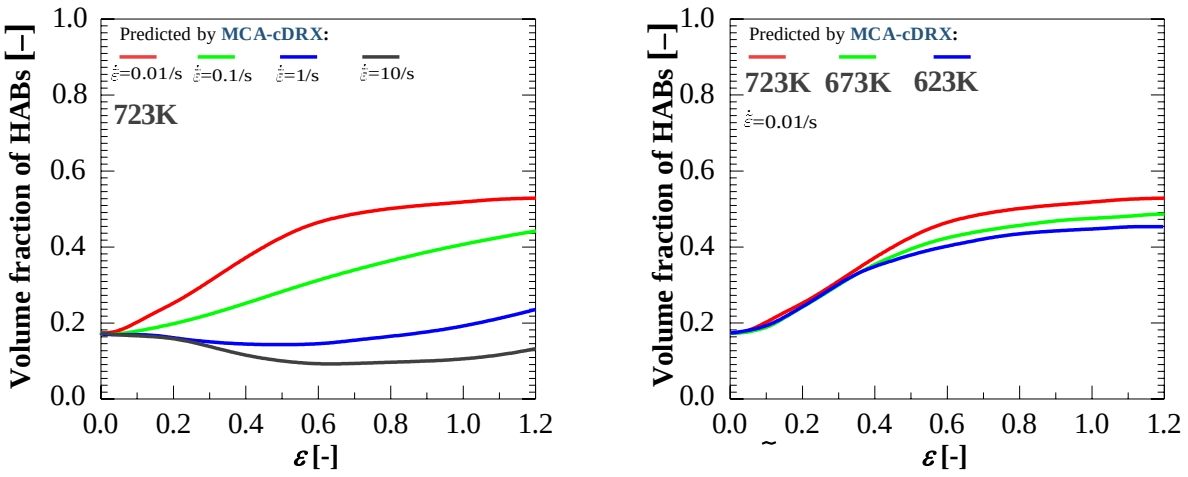

Fig. 9. The Volume fraction of HABs obtained using MCA simulation under different deformation conditions

Moreover, the volume fraction of HABs shows the following characteristics: (1) a low strain rate (e.g., $0.01s^{-1}$) offers sufficient time for the dislocation movement and rearrangement and facilitates the development of subgrain rotation, which further increases of the volume fractions of HABs with straining; (2) a high strain rate (e.g., 10 s^{-1}) effectively inhibits the migration of HABs, leading to an initial decrease in the volume fractions of HABs. As the strain increases, this value increases owing to the rotation of subgrains with respect to their neighbors and the migration of LABs, and a part of the LABs gradually reaches the critical value θ_m, which results in a transformation to HABs by trapping mobile dislocations, finally leading to an increase in the volume fractions of HABs.

As shown in Fig. 9, it is observed that the volume fraction of HABs tends to become saturation after a period of nonlinear growth. The stable value is about 40% under different deformation conditions for AA 7075 aluminum alloy. The simulated results agree well with the experimental saturation value of HABs for Al-Zn-Cu-Mg alloys (Li et al., 2020).

4.6. Influence of initial grain structure on the cDRX mechanism

4.6.1. Same sized matrix with different volume fraction of LABs

As emphasized by Gourdet and Montheillet (2003), the subgrain boundary characteristics perform a key role in controlling the progress of cDRX.

To study the effects of the initial volume fraction of LABs on the cDRX mechanism, the simulated microstructures, evolution of average subgrain size and recrystallized volume fractions under a wide range of initial deformation conditions are illustrated in Fig. 10. As shown in the figure, the initial matrix is the same as the result in Fig. 3(b1) but with different volume fractions of LABs (f_{LABs}) of 38.15 and 92.12 %, as shown in Fig. 10(a1) and (b1), respectively. The simulated microstructures are shown in Fig. 10(a2) and (b2). Further, Fig. 10(c) depicts the evolution of the average subgrain size with different values of initial f_{LABs}.

It is noteworthy that the average subgrain sizes of 6.31 μm (f_{LABs}=39.18%) and 6.85 μm (f_{LABs}=92.12%) are almost independent of the initial f_{LABs} value, whereas the evolution behavior of the subgrain and recrystallization kinetics are significantly affected by f_{LABs}. Generally, a high value of f_{LABs} is propitious for the production of cDRX and accelerates the formation of new subgrains. A potential reason for this is that a high initial f_{LABs} can promote a sufficient accumulation of mobile dislocations, leading to the formation of subgrains, which also results in a progressive increase in the misorientations of new subgrains and accelerates the formation of HABs. This mechanism has also been observed in an Al-Zr alloy (Lyttle and Wert, 1994).

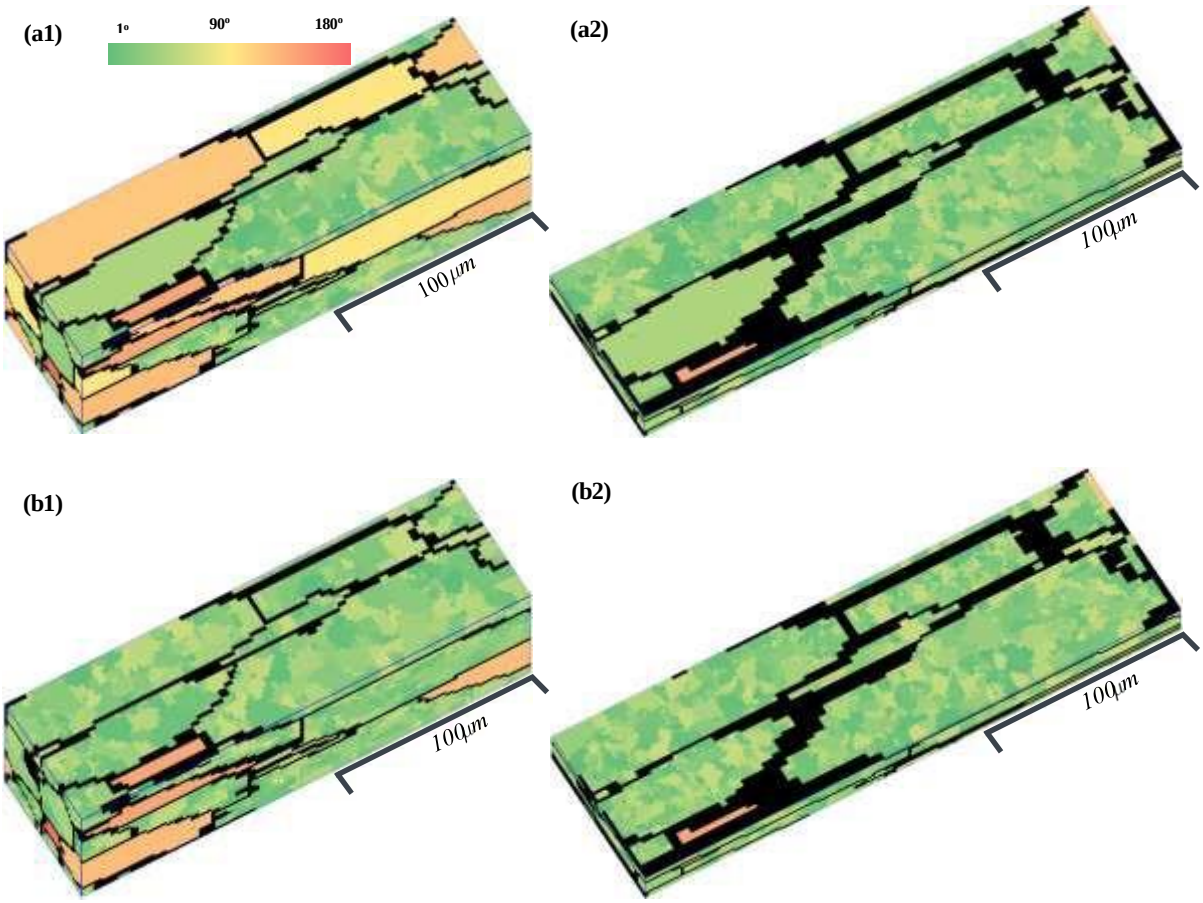

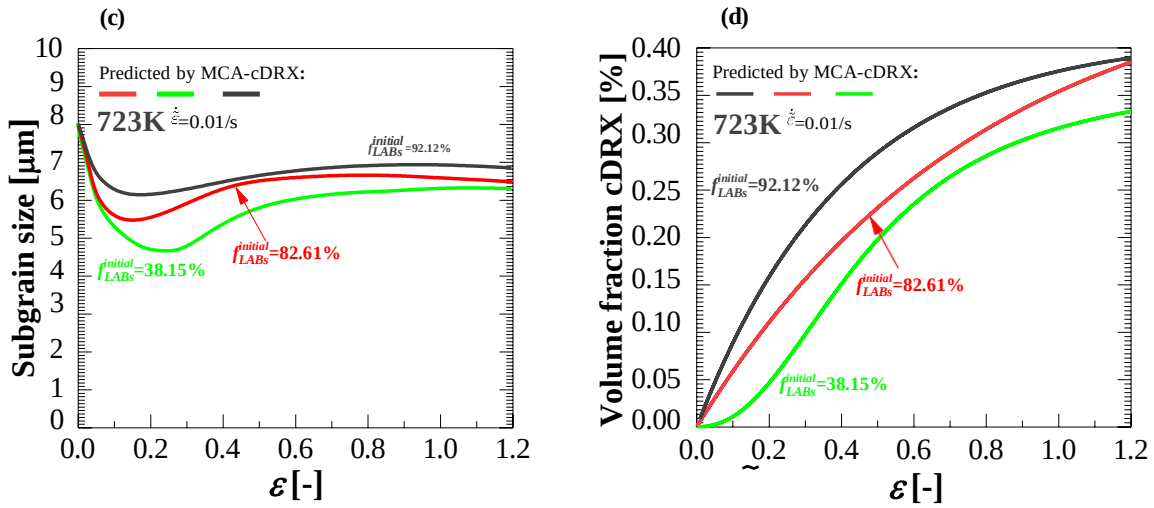

Fig. 10. Predicted microstructures of AA7055 aluminum alloy at 723K with a strain rate of 0.01 s^{-1} generated by MCA simulations. The initial volume fractions of the LABs are (a1) 38.15% and (b1) 92.12%. (a2) and (b2) are the simulated microstructures at a strain of 1.2. (c) and (d) are the evolution of average subgrain size and recrystallized volume fraction with different initial volume fractions of LABs

4.6.2. Influence of the matrix size on the cDRX mechanism

Figure 11 further shows the relation between the initial matrix and the cDRX behavior of AA7075 aluminum alloy. As an example, the initial matrix with an average grain size of 36 μm was constructed using the developed MCA-cDRX model, as shown in Fig. 11(a1). With the help of the topology deformation technique, the coupled elongated matrix and equiaxed subgrains were obtained, as shown in Fig. 11(c1), and the initial subgrain size and the volume fraction of subgrains were measured to be 8 μm and 82.61%, respectively, which are identical to those shown in Fig. 3.

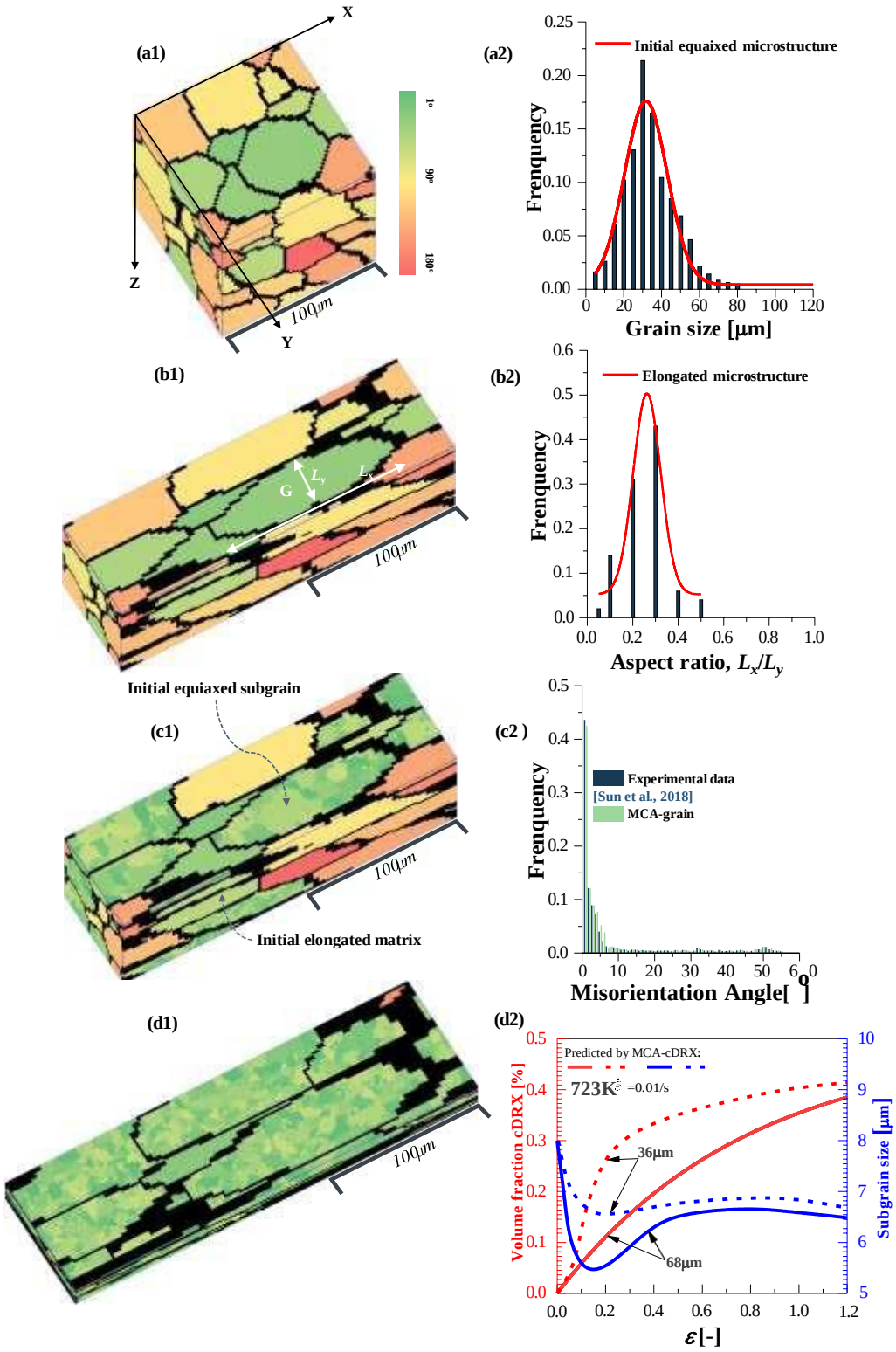

Fig. 11. (a1) Equiaxed initial microstructure with an average grain size of 36μm, (a2) grain size distribution, (b1) elongated microstructure after extrusion cogging, (b2) aspect ratio L_y/L_x distribution, (c1) initial coupled microstructures, (c2) orientation distribution of misorientation angle, (d1) cDRX microstructure at a temperature of 723 K, strain rate of 0.01 s^{-1} and strain of 1.2, and (d2) simulated evolution of average subgrain size and recrystallized volume fraction

The simulated microstructure is shown in Fig. 11(d1). By comparing different initial matrix conditions, as shown in Fig. 11(d2), it was determined that cDRX can be promoted by a fine-grain matrix because a stronger accumulation of dislocations in the dislocation cell walls through climb and cross-slip mechanisms in the deformed aluminum alloy may be achieved.

Another interesting finding of these simulations is that the initial matrix is not completely replaced by the newly formed subgrains and recrystallized grains even at a strain of 1.2. A possible reason for this is that the development of microsharp and kink bands are inhibited with certain grain orientations (Sakai et al., 2014).

4.7. The applicability of the MCA-cDRX model

The proposed MCA-cDRX model can quantify the subgrain formation and LABs migration during hot working of the materials characterized with high SFE (e.g. Al-Cu alloy and Al-Mg alloy). One issue needs to perfect for future modeling work. It is beneficial to include the effects of different types of the second-phase on the microstructure evolution during hot working. What's more, note that recrystallization texture plays an important role in determining the subsequent constitutive response during hot deformation of the materials (McQueen, 2004; Sakai et al., 2014; Chen et al., 2020). The present MCA-cDRX model cannot solve the issue perfectly. There are at least two aspects that need to be further strengthened. On the one hand, 3D EBSD technique (Witzen et al., 2020) can be employed to obtain the initial orientations of the specimen, which are then mapped into the cell space to guarantee more real orientation transformation during MCA simulation. On the other hand, more sophisticated cell type (e.g. truncated octahedral) may be introduced to realize the rotation of the subgrain with the change of the orientation.

In practice, even for the same material, the dominant mechanism may change from cDRX to dDRX and gDRX (Huang and Logé, 2016), or co-existence of three types of mechanisms under different deformation conditions (Tam et al., 2021). To this end, MCA-cDRX model coupled with the dDRX and gDRX models can be used to describe the complex microstructure evolution. Additionally, it is more meaningful to apply the proposed model to the actual hot forming (e.g. hot rolling, hot forging and hot extrusion) of the materials with high SFE. In that case, the microstructure evolution can be quantitatively simulated for heterogeneous and non-isothermal deformation. This modeling idea has been proposed and the readers interested in the details are referred to Chen et al. (2021).

Finally, plastic heterogeneity plays a significant role in progressing of DRX (Zhao et al., 2016; 2018). A dislocation density evolution model characterized by the effects of subgrain geometry and individual orientation can be further developed. In that case, plastic heterogeneity may be involved in the MCA models of DRX. The limitation will be addressed in our future work.

5. Conclusions

A new MCA-cDRX model coupled with the matrix topology deformation technique was proposed to capture the substructure evolution and macroscopic mechanical response features of materials with high SFE. The modeling studies focus on the grassroots of cDRX dynamics, emphasizing the local interaction among the cellular cells that results in a better understanding of substructure evolution mechanism during the hot working of materials. This model takes advantage of the computation performance of the MCA method for considering the effective recrystallization nucleation and subgrain growth and for achieving the visual simulation of cDRX. Moreover, the developed model is capable of modeling the substructure evolution and mechanical response of materials under large strain. The simulation results were verified through the uniaxial hot compression of AA7075 aluminum alloy, and its mesoscale mechanisms were revealed:

(1) The subgrain size is inversely proportional to the Zener-Hollomon parameter, whose higher value leads to more fully polygonized subgrains. This dynamic simulation offers a new way to understand the subgrain evolution due to cDRX.

(2) It was suggested that the incubation time for subgrains formation is significantly short, resulting in quick hardening behavior of the material accompanied by a peak value of the flow stress.

(3) The effect of the initial characteristics of the matrix was highlighted, and their special roles on the cDRX kinetics were captured. It was observed that both the fine-grain matrix and high f_{LABs} could accelerate the cDRX process. The relationship between the initial matrix and recrystallized fraction and subgrain size were obtained.

(4) It was predicted that the MCA-cDRX shows a saturation value of f_{HABs}. In particular, the temperature has demonstrated a significantly lower effect on f_{HABs} than the strain rate in the investigated Zener-Hollomon parameter range.

CRediT authorship contribution statement

Fei Chen: Funding acquisition, Project administration, Conceptualization, Methodology, Visualization, Writing-original draft. **Xiao Tian:** Data curation. **Guangshan Wu:** Data curation. **Huajia Zhu:** Conceptualization, Writing-review & editing. **Hengan Ou:** Methodology, Writing-review & editing. **Zhenshan Cui:** Methodology, Conceptualization, Writing-review & editing.

Declaration of interests

The authors declare that they have no known competing financial interests or personal relationships that could have appeared to influence the work reported in this paper.

Acknowledgements

This work is supported by the National Natural Science Foundation of China (grant number: U2037204).

Appendix A- Key factors of MCA

Appendix A1-Cellular state switching rules for generating the initial equiaxed microstructure

GB migration is a thermally activated process that involves the movement of an atom or a group of atoms from one grain to its neighbor across a GB (McQueen, 2004). Based on this theory, the cells with energy greater than the activation energy may be changed to a new state/orientation at a given temperature. Therefore, at each CA step, the cells change their state/orientation according to the probability $P_{i\_thermal} = \exp(-Q_b / RT)$.

Several experimental and theoretical studies have confirmed that the curvature-driven mechanism performs a key role in grain growth (Sakai et al., 2014). According to this theory, the following rules were established to achieve the state/orientation change during grain growth controlled by the curvature mechanism. As shown in Fig. A1, if three or more arbitrary cells in the von Neumann neighborhood have the same orientations, which is recorded as O , the orientation of the central cell transforms to O in the next time step.

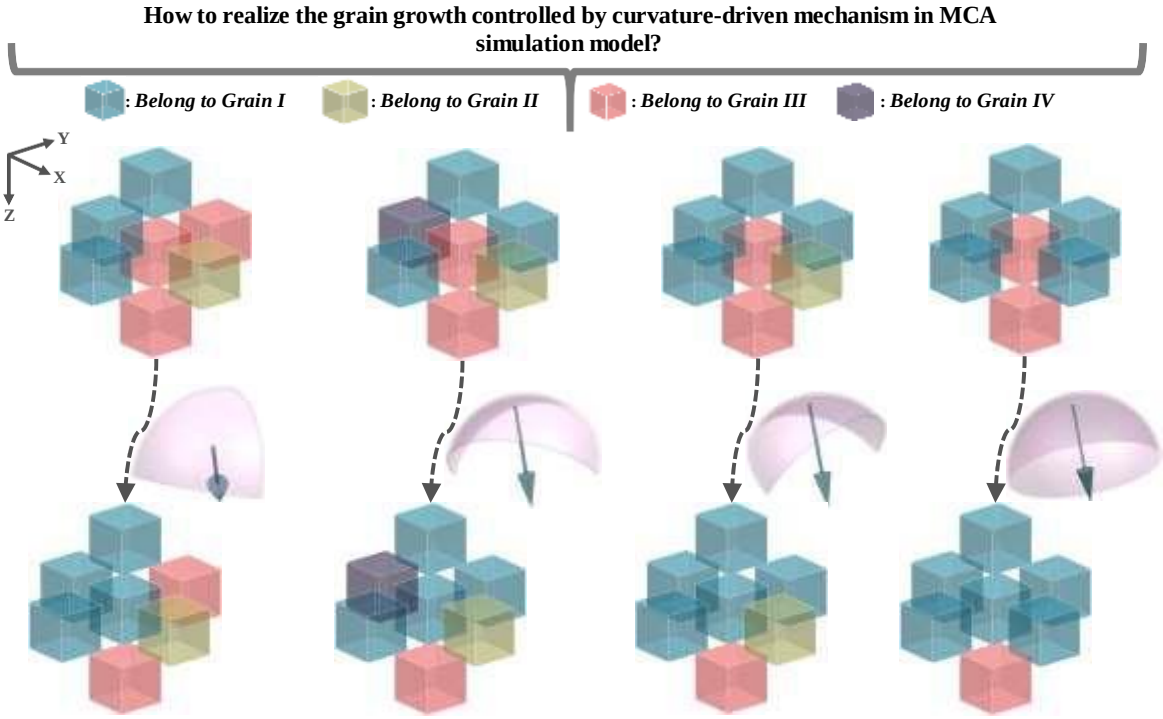

Fig. A1. Schematic for achieving GB migration driven by curvature

When the initial microstructure is generated, if it does not satisfy the above switching rules, the state/orientation of the central cell will randomly translate to an arbitrary state of the von Neumann neighborhood. Based on the minimization principle of energy (Barmak et al., 2006), if the total energy of a local small system (a total of seven cells) is reduced after the trial transition, then a change occurs. Here, the energy change after the trial transition is calculated

by $\Delta E = E_j - E_i$, where $E_i = J\sum_{n}^{\chi_{von}}[1-\delta(O_i O_n)]$, J is a measurement for GB energy, which is equal to 1 in this study, δ is the Kronecker symbol, n is the *nth* neighbor to the central cell i, χ_{von} indicates the total neighbors of the central cell i, and its value is six considering the von Neumann configuration. O_i is the orientation of the central cell i, O_n is the orientation of the cell that is a neighbor of cell i, and j refers to one of the neighbors of the central cell. Therefore, the probability of the trial transition (supposing $O_i = O_j$) is equal to 1 if $\Delta E < 0$; if not, the transition does not occur.

Appendix A2-Topology deformation technique in 3D MCA simulation

The deformation of grain shape results in changes in the GB, which demonstrates a powerful influence on subgrain formation, rotation, and growth during DRX. To describe the effect of topology deformation on the grain shape more accurately, two coordinate systems with the cellular/material coordinate systems were used (Chen et al., 2010). During hot working, the cellular coordinate system remains unchangeable; however, the material coordinate system and the corresponding GB topology will change with deformation. Thus, the dimension of the cell remains unchanged within the cellular coordinate system, but it will change with deformation within the material coordinate system. The details of this method can be referred to in our previous work (Chen et al., 2012; 2014).

Figure A2 shows two examples of the manner in which the dimension of cells can be calculated in the application of the topology deformation technique in MCA simulation of cDRX. As shown in Fig. A2-I, the initial cellular space was set as $50 \times 50 \times 50$, corresponding to the computation volume of 100 μm×100 μm×100 μm in the real deformed billet. This implies that $N_{x\_cell} = N_{y\_cell} = N_{z\_cell} = 50$ and $l_x = l_y = l_z = 2\mu m$. To prevent the loss of the neighboring cells in the 3D cellular space, periodic boundary conditions were used to reduce the interface effects (Chen et al., 2021). The grain deformation can be transformed into the deformation of the cube within the grain in 3D MCA. It can be described as follows:

$$\begin{pmatrix} f_x \\ f_y \\ f_z \end{pmatrix} = \begin{pmatrix} S_{11} & S_{12} & S_{13} \\ S_{21} & S_{22} & S_{23} \\ S_{31} & S_{32} & S_{33} \end{pmatrix} \begin{pmatrix} l_x \\ l_y \\ l_z \end{pmatrix} \quad \text{(B1)}$$

where l_x, l_y, l_z are the original dimensions of the cell and f_x, f_y, f_z are the new dimensions of the cell after deformation. The elements of the deformation matrix, $\boldsymbol{S}$, are determined according to the type of deformation.

Cogging in the rolling of aluminum ingots (Fig. A2-R) can be approximately considered that as a type of plane-strain problem because the length of the workpiece is far more than its width; consequently, the width stays the same. Thus, all the elements are 0, except for the

diagonal elements S_{11} and S_{33}, which are the principle normal deformations in the X and Z directions, respectively, which are the ratios of the final and initial length along these two axes. Therefore, $\tilde{\varepsilon}_x = \ln S_{11}$ and $\tilde{\varepsilon}_z = \ln S_{33}$ are the true strains along the two principal axes. As the volume remains constant during deformation, the determinant must be a unit value ($S_{11}S_{33} = 1$).

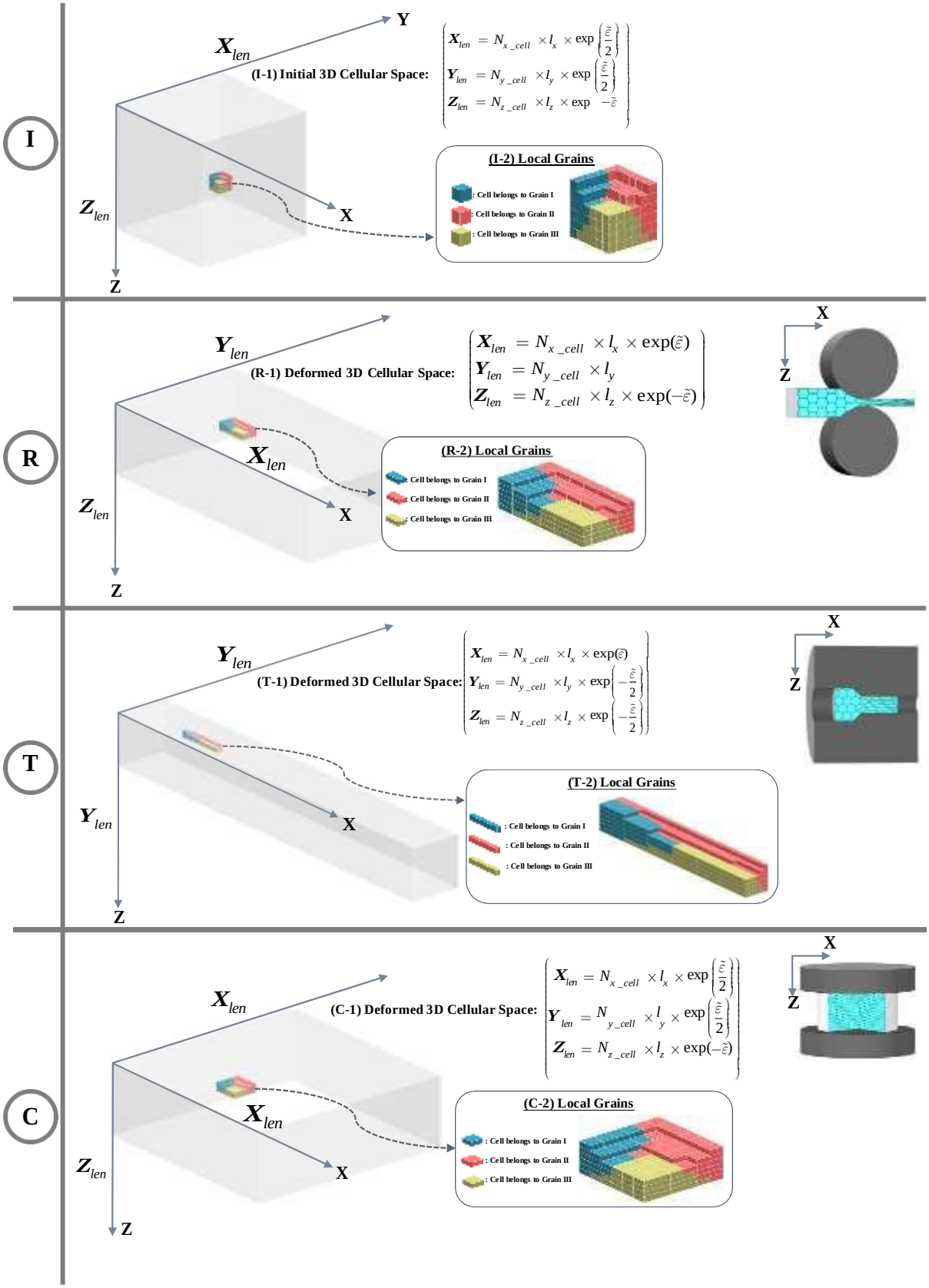

Fig. A2. Schematic for achieving of grain topology deformation. (I) represents the initial state, (R) represents the rolling state, (T) represents the extrusion state and (C) represents the axial compression state

However, for the axial compression of the samples (Fig. A2-C), all the elements are 0, except for the diagonal elements S_{11}, S_{11}, and S_{33}. Here, it is assumed that the true strain is $\tilde{\varepsilon}$, $f_z = l_z \exp(-\tilde{\varepsilon})$, $f_x = l_x \exp(\tilde{\varepsilon}/2)$ and $f_y = l_y \exp(\tilde{\varepsilon}/2)$.

References

Aukrust, T., Tjøtta, S., Vatne, H.E., Houtte, P. Van., 1997. Coupled FEM and texture modelling of plane strain extrusion of an aluminum alloy. Int. J. Plast. 13, 111-125. https://doi.org/10.1016/S0749-6419(97)00003-X.

Avramovic-Cingara, G., Perovic, D.D., McQueen, H.J., 1996. Hot deformation mechanisms of a solution-treated Al-Li-Cu-Mg-Zr alloy. Metall. Mater. Trans. A 27, 3478-3490. https://doi.org/10.1007/BF02595440.

Barmak, K., Kim, J, Kim, C.-S., Archibald, W.E., Rohrer, G.S., Rollett, A.D., Kinderlehrer, D., Taasan, S., Zhang, H., Srolovitz, D.J., 2006. Grain boundary energy and grain growth in Al films: Comparison of experiments and simulations. Scirpta Mater. 54, 1059-1063. https://doi.org/10.1016/j.scriptamat.2005.11.060.

Beer, A.G., Barnett, M.R., 2007. Microstructural development during hot working of Mg-3Al-1Zn. Metall. Mater. Tran. A, 38, 1856-1768. https://doi.org/10.1007/s11661-007-9207-5.

Borodin, E.N., Mayer, A.E., Gutkin, M.Yu., 2020. Coupled model for grain rotation, dislocation plasticity and grain boundary sliding in fine-grianed solids. Int. J. Plast. 134, 102776. https://doi.org/10.1016/j.ijplas.2020.102776.

Beucia, B., Queyreau, S., Kahloun, C., Chaubet, D., Franciosi, P., Bacroix, B. 2018. Plastic strain-induced grain boundary migration (SIBM) in pure aluminum:SEM in-situ and AFM examinations. Int. J. Plast. 115, 29-55. https://doi.org/10.1016/j.ijplas.2018.11.007.

Buzolin, R.H., Lasnik, M., Krumphals, A., Poletti, M.C., 2021. A dislocation-based model for the microstructure evolution and the flow stress of a Ti5553 alloy. Int. J. Plast. 136, 102862. https://doi.org/10.1016/j.ijplas.2020.102862.

Busso, E.P., 1998. A continuum theory for dynamic recrystallization with microstructure-related length scales. Int. J. Plast. 14, 319-353. https://doi.org/10.1016/S0749-6419 (98)00008-4.

Cai, Y., Sun, C.Y., Li, Y.L., Hu, S.Y., Zhu, N.Y., Barker, E.I., Qian, L.Y., 2020. Phase field modeling of discontinuous dynamic recrystallization in hot deformation of magnesium alloys. Int. J. Plast. 133, 102773. https://doi.org/10.1016/j.ijplas.2020.102773.

Chen, F., Cui, Z.S., Liu, J., Zhang, X.X., Chen, W., 2009. Modeling and simulation on dynamic recrystallization of 30Cr2Ni4MoV rotor steel using the cellular automaton method. Modelling Simul. Mater. Sci. Eng. 17, 075015. https://doi.org/10.1088/0965-0393/17/7/075015.

Chen, F., Cui, Z.S., 2012. Mesoscale simulation of microstructure evolution during multi-stage hot forging processes. Model. Simul. Mater. Sci. Eng. 20, 045008. https://doi.org/10.1088/0965-0393/20/4/045008.

Chen, F., Qi, K., Cui, Z.S., Lai, X.M., 2014. Modeling the dynamic recrystallization in austenitic stainless steel using cellular automaton method. Comput. Mater. Sci. 83, 331-340. http://dx.doi.org/10.1016/j.commatsci.2013.11.029.

Chen, F., Zhu, H.J., Zhang, H.M., Cui, Z.S., 2020. Mesoscale modeling of dynamic recrystallization: Multilevel cellular automaton simulation framework. Metall. Mater. Trans. A 51, 1286-1303. https://doi.org/10.1007/s11661-019-05620-3.

Chen, F., Zhu, H.J., Chen, W., Ou, H., Cui, Z.S., 2021. Multiscale modeling of discontinuous dynamic recrystallization during hot working by coupling multilevel cellular automaton and finite element method. Int. J. Plast. 145, 103064. https://doi.org/10.1016/j.ijplas.2021.103064.

Chen, S.F., Li, D.Y., Zhang, S.H., Han, H.N., Lee, H.W., Lee, M.G., 2020. Modelling continuous dynamic recrystallization of aluminium alloys based on the polycrystal plasticity approach. Int. J. Plast. 131, 102710. https://doi.org/10.1016/j.ijplas.2020.102710.

Cho, H.E., Hammi, Y., Bowman, A.L., Karato, S.-I., Baumgardner, J.R., Horstemeyer, M.F., 2019. A unified static and dynamic recrystallization Internal State Variable (ISV) constitutive model coupled with grain size evolution for metals and mineral aggregates. Int. J. Plast. 112, 123-157. https://doi.org/10.1016/j.ijplas.2018.08.009.

Ding, R., Guo, Z.X., 2001. Coupled quantitative simulation of microstructural evolution and plastic flow during dynamic recrystallization. Acta Mater. 49, 3163-3175.https://doi.org/10.1016/S1359-6454(01)00233-6.

Doherty, R.D., Hughes, D.A., Humphreys, F.J., Jonas, J.J., JuulJensen, D., Kassner, M.E., King, W.E., McNelley, T.R., McQueen, H.J., Rollett, A.D., 1997. Current issues in recrystallization: a review. Mater. Sci. Eng. A 238, 219-274. https://doi.org/10.1016/S0921-5093(97)00424-3.
Doherty, R.D., Szpunar, J.A., 1984. Kinetic of sub-grain coalescence-A reconsideration of the theory. Acta Metall. 32, 1789-1798. https://doi.org/10.1016/0001-6160(84)90235-9.
Donati, L., Segatori, A., Mehtedi, M.E., Tomesani, L., 2013. Grain evolution analysis and experimental validation in the extrusion of 6XXX alloys by use of a lagrangian FE code. Int. J. Plast. 46, 70-81. https://doi.org/10.1016/j.ijplas.2012.11.008.
Driver, J., 2018. The limitations of continuous dynamic recrystallization (CDRX) of aluminium alloys. Mater. Lett. 222, 135-137. https://doi.org/10.1016/j.matlet.2018.03.196.
Duan, X., Sheppard, T. 2002. Three dimensional thermal mechanical coupled simulation during hot rolling of aluminium alloy 3003. Int. J. Mech. Sci. 44, 2155-2172. https://doi.org/10.1016/S0020-7403(02)00164-9.
Estrin, Y., Tóth, L.S., Molinari, A., Bréchet, Y., 1998. A dislocation-based model for all hardening stages in large strain deformation. Acta Mater. 46, 5509-5522. https://doi.org/10.1016/S1359-6454(98)00196-7.
Fan, X.G., Yang, H., 2011. Internal-state-variable based self-consistent constitutive modeling for hot working of two-phase titanium alloys coupling microstructure evolution. Int. J. Plast. 27, 1833-1852. https://doi.org/10.1016/j.ijplas.2011.05.008.
Fratini, L., Buffa, G., 2005. CDRX modelling in friction stir welding of aluminium alloys. Int. J. Mach. Tool. Manu. 45, 1188-1194. https://doi.org/10.1016/j.ijmachtools.2004.12.001.
Gourdet, S., 1997. Etude des mécanismes de recristallisation au cours de la déformation à chaud de l'aluminium. Ecole Nationale Sup′erieure des Mines de Saint-Etienne.
Gourdet, S., Montheillet, F., 2003. A model of continuous dynamic recrystallization. Acta Mater. 51, 2685-2699. https://doi.org/10.1016/S1359-6454(03)00078-8
Gottstein, G., 2004. Physical foundations of materials science (1st ed.). Springer Verlag, Berlin.
Hallberg, H., Wallin, M., Ristinmaa, M., 2010. Modeling of continuous dynamic recrystallization in commercial-purity aluminum. Mater. Sci. Eng. A 527, 1126-1134. https://doi.org/10.1016/j.msea.2009.09.043.
Gupta, R.K., Kumar, V.A., Krishnan, A.S., Niteshraj, J., 2019. Hot deformation behavior of aluminum alloys A7010 and AA7075. J. Mater. Eng. Perform. 28, 5021-5036. https://doi.org/10.1007/s11665-019-04231-8.
Huang, K., Logé, R.E., 2016. A review of dynamic recrystallization phenomena in metallic materials. Mater. Des. 111, 548-574. https://doi.org/10.1016/j.matdes.2016.09.012.
Huang, Y., Humphreys, F.J., 2000. Subgrain growth and low angle boundary mobility in aluminium crystals of orientation {110}<001>. Acta Mater. 48, 2017-2030. https://doi.org/10.1016/S1359-6454(99)00418-8.
Humphreys, F., Hatherly, M., 2004. Recrystallization and related annealing phenomena, second ed. Elsevier Ltd, Oxford.
Janssens, K.G.F., 2010. An introductory review of cellular automata modeling of moving grain boundaries in polycrystalline materials. Math. Comput. Simul. 80,1361-1381. https://doi.org/10.1016/j.matcom.2009.02.011.
Jazaeri, H., Humphreys, F.J., 2004. The transition from discontinuous to continuous recrystallization in some aluminium alloys:I-the deformed state. Acta Mater. 52, 3239-3250. https://doi.org/10.1016/j.actamat.2004.03.030.
Jägle, E.A., Mittemeijer, E.J., 2012. Interplay of kinetics and microstructure in the recrystallization of pure copper: comparing mesoscopic simulations and experiments. https://doi.org/10.1007/s11661-012-1094-8.
Jr., Misiolek. 2008. Theoretical predictions and experimental verification of surface grain structure evolution for AA6061 during hot rolling. Acta Mater. 56, 6174-6185. https://doi.org/10.1016/j.actamat.2008.08.050.
Khan, A.S., Pandey A., Gnäupel-Herold, T., Mishra, R.K., 2011. Mechanical response and texture evolution of AZ31 alloy at large strains for different strain rates and temperatures. Int. J. Plast. 27, 688-706. https://doi.org/10.1016/j.ijplas.2010.08.009.
Khan, A.S., Meredith, C.S., 2010. Thermo-mechanical response of Al 6061 with and without equal channel angular pressing (ECAP). Int. J. Plast. 26, 189-203. https://doi.org/10.1016/j.ijplas.2009.07.002.
Khan, A.S., Baig, M., 2011. Anistropic response, constitutive modeling and the effects of strain-rate and temperature on the formability of an aluminum alloy. Int. J. Plast. 27, 522-538. https://doi.org/10.1016/j.ijplas.2010.08.001.
Kugler, G., Turk, R., 2004. Modeling the dynamic recrystallization under multi-stage hot deformation.

Acta Mater. 52, 4659-4668. https://doi.org/10.1016/j.actamat.2004.06.022.
Laasraoui, A., Jonas, J.J. 1991. Prediction of steel flow stresses at high temperatures and strain rates. Metall. Trans. A 22, 1545-1558. https://doi.org/10.1007/BF02667368.
Li, H., Fu, M.W., 2018. Deformation Based Processing of Materials:Behavior, Performance, Modelling, and Control. Elsevier, Mar, 2019. https://doi.org/10.1016/C2017-0-01559-8.
Li, H., Wu, C., Yang, H., 2013. Crystal plasticity modeling of the dynamic recrystallization of two-phase titanium alloys during isothermal processing. Int. J. Plast. 51,271-291. https://doi.org/10.1016/j.ijplas.2013.05.001.
Li, H., Sun, X., Yang, H., 2016. A three-dimensional cellular automata-crystal plasticity finite element model for predicting the multiscale interaction among heterogeneous deformation, DRX microstructural evolution and mechanical response in titanium alloys. Int. J. Plast. 2016, 154-180. https://doi.org/10.1016/j.ijplas.2016.09.008.
Li, Y.B., Gu, B., Jiang, S., Liu, Y.Q., Shi, Z.S., Lin, J.G., 2020. A CDRX-based material model for hot deformation of aluminium alloys. Int. J. Plast. 134, 102844. https://doi.org/10.1016/j.ijplas.2020.102844.
Liu, L., Wu, Y.X., Ahmad, A.S., 2021. A novel simulation of continuous dynamic recrystallization process for 2219 aluminum alloy using cellular automata technique. Mater. Sci. Eng. A 815: 141256. https://doi.org/10.1016/j.msea.2021.141256.
Lyttle, M.T., Wert, J.A., 1994. Modelling of continuous recrystallization in aluminium alloys. J. Mater. Sci. 29, 3342-3350. https://doi.org/10.1007/BF00356683.
Mahnken, R., Westermann, H., 2021. A non-equilibrium thermodynamic framework for viscoplasticity incorporating dynamic recrsytallization at large strains. Int. J. Plast. 142, 102988. https://doi.org/10.1016/j.ijplas.2021.102988.
Maizza, G., Pero, R., Richetta, M., Montanari, R., 2018. Continuous dynamic recrystallization (CDRX) model for aluminium alloys. J Mater. Sci. 53, 4563-4573. https://doi.org/10.1007/s10853-017-1845-4.
Mallick, A., Vedantam, S., 2009. Phase field study of the effect of grain boundary energy anisotropy on grain growth. Comp. Mater. Sci. 46, 21-25. https://doi.org/10.1016/j.commatsci.2009.01.026.
McQueen, H.J., Hockett, E., 1970. Microstructures of aluminum compressed at various rates and temperatures. Metall. Trans. 1, 2997-3004. https://doi.org/10.1007/BF03038412.
McQueen, H.J., 2004. Development of dynamic recrystallization theory. Mater. Sci. Eng. A 387-389, 203-208. https://doi.org/10.1016/j.msea.2004.01.064.
McQueen, H.J., Kassner, M.E., 2004. Comments on a model of continuous dynamic recrystallization proposed for aluminum. Scr. Mater. 51, 461-465. https://doi.org/10.1016/j.scriptamat.2004.05.027.
McQueen, H.J., Spigarelli, S., Kassner, M.E., Evangelista, E., 2010. Hot deformation and processing of aluminum alloy. CRC Press, 2010.
Moldovan, D., Yamakov, V., Wolf, D., Phillpot, S.R., 2002. Scaling behavior of grain-rotation-induced grain growth. Phys. Rev. Lett. 89:206101. https://doi.org/10.1103/PhysRevLett.89.206101.
Nayan, N., Mahesh, S., Prasad, M.J.N.V., Murthy, S.V.S.N., Samajdar, I., 2019. A phenomenological hardening model for an aluminium-lithium alloy. Int. J. Plast. 118, 215-232. https://doi.org/10.1016/j.ijplas.2019.02.009.
Prangnell, P.B., Bate, P.S., 2007. Subgrian rotation recrystallization in minerals. Mater. Sci. Forum, 550, 95-104. https://doi.org/10.4028/www.scientific.net/MSF.550.95.
Raabe, D., 1999. Introduction of a scalable three-dimensional cellular automaton with a probabilistic switching rule for the discrete mesoscale simulation of recrystallization phenomena. Philos. Mag. A 79, 2339-2358. https://doi.org/10.1080/01418619908214288.
Raabe, D., 2002. Cellular automata in materials science with particular reference to recrystallization simulation. Annu. Rev. Mater. Sci. 32, 53-76. https://doi.org/10.1146/annurev.matsci.32.090601.152855.
Roters, F., Raabe, D., Gottstein, G., 2000. Work hardening in heterogeneous alloys-a microstructural approach based on three internal state variables. Acta Mater. 48, 4181-4189. https://doi.org/10.1016/S1359-6454(00)00289-5.
Read, W.T., Shockley, W., 1950. Dislocation models of crystal grain boundaries. Phys. Rev. 78, 275.
Roberts, W., Ahlblom, B., 1978. A nucleation criterion for dynamic recrystallization during hot working. Acta Metall. 26, 801–813. https://doi.org/10.1016/0001-6160(78)90030-5.
Sakai, T., Belyakov, A., Kaibyshev, R., Miura, H., Jonas, J.J., 2014. Dynamic and post-dynamic recrystallization under hot, cold and severe plastic deformation conditions. Prog. Mater. Sci. 60, 130-207. https://doi.org/10.1016/j.pmatsci.2013.09.002.
Sellars, C.M., in:B.Hutchinson et al. (Eds.), 1996. Thermomechanical Processing in Theory, Modelling and Practice [TMP]^2, ASM Stockholm, Sweden.
Sellars, C.M., Zhu, Q., 2000. Microstructure modelling of aluminium alloys during thermomechanical processing. Mater. Sci. Eng. A 280, 1-7. https://doi.org/10.1016/S0921-5093(99)00648-6.

Siu, K.W., Ngan, A.H.W., Jones, I.P., 2011. New insight on acoustoplasticity-Ultrasonic irradiation enhances subgrain formation during deformation. Int. J. Plast. 27, 788-800. https://doi.org/10.1016/j.ijplas.2010.09.007.
Smith, L.T.W., Su, Y.Q, Xu, S.Z., Hunter, A., Beyerlein I.J. 2020. The effect of local chemical ordering on Frank-Read source activation in a refractory multi-principle element alloy. Int. J. Plast. 134:102850. https://doi.org/10.1016/j.ijplas.2020.102850.
Sun, Z.C., Wu, H.L., Cao, J., Yin, Z.K., 2018. Modeling of continuous dynamic recrystallization of Al-Zn-Cu-Mg alloy during hot deformation based on the internal-state-variable (ISV) method. Int. J. Plast. 106, 73-87. https://doi.org/10.1016/j.ijplas.2018.03.002.
Sun, Z.C., Zheng, L.S., Yang, H., 2014. Softening mechanism and microstructure evolution of as-extruded 7075 aluminum alloy during hot deformation. Mater. Charact. 90, 71-80. http://dx.doi.org/10.1016/j.matchar.2014.01.019.
Svyetlichnyy, D.S., 2010. Modelling of the microstructure: from classical cellular automata approach to the frontal one. Comput. Mater. Sci. 50, 92-97. https://doi.org/10.1016/j.commatsci.2010.07.011.
Svyetlichnyy, D.S., 2014. A three-dimensional frontal cellular automaton model for simulation of microstructure evolution-initial microstructure module. Model. Simul. Mater. Sci. Eng. 22, 085001 https://doi.org/10.1088/0965-0393/22/8/085001.
Tam, K.J, Vaughan, M.W., Shen, L.M., Knezevic, M., Karaman, I., Proust, G., 2021. Modeling dynamic recrystallization in magnesium alloy AZ31. Int. J. Plast. 142, 102995. https://doi.org/10.1016/j.ijplas.2021.102995.
Takaki, T., Yoshimoto, C., Yamanaka, A., Tomita, Y., 2014. Multiscale modeling of hot-working with dynamic recrystallization by coupling microstructure evolution and macroscopic mechanical behavior. Int. J. Plast. 52, 105-116. https://doi.org/10.1016/j.ijplas.2013.09.001.
Tu, X.H., Shahba, A., Shen, J.L., Ghosh, S., 2019. Microstructure and property based statistically equivalent RVEs for polycrystalline-polyphase aluminum alloys. Int. J. Plast. 115, 268-292. https://doi.org/10.1016/j.ijplas.2018.12.002.
Tóth, L.S., Estrin, Y., Lapovok, R., Gu, C.F., 2010. A model of grian fragementation based on lattice curvature. Acta Mater. 58, 1782-1794. https://doi.org/10.1016/j.actamat.2009.11.020.
Vatne, H.E., Furu, T., Ørsund, R., Nes, E., 1996. Modeling recrystallization after hot deformation of aluminium. https://doi.org/10.1016/1359-6454(96)00078-X.
Winning, M., Rollett, A.D., Gottstein, G., Srolovitz, D.J., Shvindlerman, A. Lim & L.S., 2010. Mobility of low-angle grain boundaries in pure metals. Philos. Mag. 90:3107-3128. https://doi.org/10.1080/14786435.2010.481272.
Witzen, W.A., Polonsky, A.T., Pollock, T.M., Beyerlein, I.J., 2020. Three-dimensional maps of geometrically necessary dislocation densities in additively manufactured Ni-based superalloy IN718. Int. J. Plast. 131, 102709. https://doi.org/10.1016/j.ijplas.2020.102709.
Yamagata, H., Ohuchida, Y., Saito, N., Otsuka, M., 2001. Nucleation of new grains during discontinuous dynamic recrystallization of 99.998 mass% Aluminum at 453 K. Scripta Mater. 45, 1055-1061. https://doi.org/10.1016/S1359-6462(01)01139-3.
Yang, Q.Y., Deng, Z.H., Zhang, Z.Q., Liu, Q., Jia, Z.H., Huang, G.J, 2016. Effects of strain rate on flow stress behaviour and dynamic recrystallization mechanism of Al-Zn-Mg-Cu aluminum alloy during hot deformation. Mater. Sci. Eng. A 662, 204-213. https://doi.org/10.1016/j.msea.2016.03.027.
Yazdipour, N., Davies, C.H.J., Hodgson, P.D., 2008. Microstructural modeling of dynamic recrystallization using irregular cellular automata. Comput. Mater. Sci. 44, 566-576. https://doi.org/10.1016/j.commatsci.2008.04.027.
Zhao, P., Low, T.S.E., Wang, Y., Niezgoda, S.R., 2016. An integrated full-field model of concurrent plastic deformation and microstructure evolution: application to 3d simulation of dynamic recrystallization in polycrystalline copper. Int. J. Plast. 80, 38–55. https://doi.org/10.1016/j.ijplas.2015.12.010.
Zhao, P., Wang, Y., Niezgoda, S.R., 2018. Microstructural and micromechanical evolution during dynamic recrystallization. Int. J. Plast. 100, 52-68. https://doi.org/10.1016/j.ijplas.2017.09.009.
Zhen, C.W., Raabe, D., 2013. Interaction between recrystallized and phase transformation during intercritical annealing in a cold-rolled dual-phase steel: a cellular automaton model. Acta Mater. 61, 5504-517. https://doi.org/10.1016/j.actamat.2013.05.040.